Global contributions of mesoscale dynamics to meridional heat transport

Andrew Delman[1] and Tong Lee[1]

[1]Jet Propulsion Laboratory, California Institute of Technology, Pasadena, CA, USA

Correspondence: Andrew Delman (adelman@jpl.caltech.edu)

Abstract.

Mesoscale ocean processes are prevalent in many parts of the global oceans, and may contribute substantially to the meridional movement of heat. Yet earlier global surveys of temperature fluxes and meridional heat transport (~~MHT~~HT) have not formally distinguished between mesoscale and large-scale contributions, or have defined eddy contributions based on temporal rather than spatial characteristics. This work uses spatial filtering methods to separate large-scale (gyre and planetary wave) contributions from mesoscale (eddy, recirculation, and tropical instability wave) contributions to ~~MHT by extending beyond a previous effort for the North Atlantic Ocean~~meridional HT. Overall, ~~mesoscale temperature fluxes produce~~ the mesoscale temperature flux (MTF) produces a net poleward ~~MHT~~ meridional HT at mid-latitudes and equatorward ~~MHT~~ meridional HT in the tropics, thereby resulting in a net divergence of heat from the subtropics. ~~Mesoscale temperature fluxes are often concentrated near the energetic currents at western boundaries, and~~ In addition to MTF generated by propagating eddies and tropical instability waves, MTF is also produced by stationary recirculations near energetic western boundary currents, where the temperature difference between the boundary current and its recirculation ~~determines the direction of the mesoscale temperature flux~~produces the MTF. The mesoscale contribution to ~~MHT~~ meridional HT yields substantially different results from temporally-based "eddy" contributions to ~~MHT~~meridional HT, with the latter ~~contributed substantially by~~ including large-scale gyre and planetary wave motions at low latitudes. Mesoscale temperature fluxes contribute the most to interannual and decadal variability of ~~MHT~~ meridional HT in the Southern Ocean, the tropical Indo-Pacific, and the North Atlantic. Surface eddy kinetic energy (EKE) alone is not a good proxy for mesoscale temperature flux variability in regions with the highest time-mean EKE, though it does explain much of the temperature flux variability in regions of modest time-mean EKE. This approach to quantifying mesoscale fluxes can be used to improve parameterizations of mesoscale effects in coarse-resolution models, and assess regional impacts of mesoscale eddies and recirculations on tracer fluxes.

1 Introduction

Along frontal gradients in the ocean, instabilities form that exchange waters of different temperatures, resulting in heat transport across latitude lines. Many of these instabilities (eddies) assume scales comparable to or slightly larger than the baroclinic radius of deformation (e.g., Chelton et al., 2011), corresponding to the oceanic mesoscale (tens to hundreds of kilometers). In addition to eddies, tropical instability waves (TIWs; e.g., Jochum and Murtugudde, 2006) and recirculation gyres that flank boundary current jets also have the capacity to move heat meridionally in the ocean at mesoscales. Unlike the wind-forced response associated with larger-scale gyres and planetary waves, these mesoscale phenomena are generated and sustained by nonlinear mechanisms such as baroclinic and barotropic instability (e.g., Eady, 1949; Charney and Stern, 1962) and nonlinear momentum advection (e.g., Greatbatch et al., 2010).

Despite the prevalence of mesoscale features in the global oceans, relatively little attention has been given to quantifying their contributions to meridional heat transport (~~MHT~~HT) until recently. Most of the literature characterizing the oceanic ~~MHT~~ meridional HT emphasizes the dominant role of the overturning circulation (e.g., Talley, 2003), arising from the steep vertical temperature gradients at lower latitudes. Some of these studies assess the "gyre" contribution separately from the overturning (e.g., Bryan, 1982; Johns et al., 2011). In this framework, the overturning contribution is the integrated product of the zonal mean meridional velocity v and temperature T, and the gyre contribution consists of the residual (zonally-varying) v and T. However, no distinction is made between the temperature flux associated with the basin-scale gyres vs. smaller mesoscale processes. This distinction is important not only because the forcing mechanisms for basin-scale motions are quite different from mesoscale motions, but also because the coarse-resolution oceans in most climate model simulations do not explicitly represent mesoscale motions and must parameterize their effects. In recent years, eddy tracking and identification methods (e.g., Chaigneau and Pizarro, 2005; Chelton et al., 2011; Laxenaire et al., 2018) have been used to quantify the specific ~~MHT~~ meridional HT or temperature flux contributions of identified eddies (e.g., Hausmann and Czaja, 2012; Dong et al., 2014, 2017; Sun et al., 2019; Müller et al., 2019; Laxenaire et al., 2020). Yet not all mesoscale flow features take the form of coherent vortices, and the actual movement of coherent eddies likely accounts for a relatively small portion of the fluxes associated with the mesoscale ~~(e.g., Hausmann and Czaja, 2012; Abernathey and Haller, 2018)~~ (e.g., Hausmann and Czaja, 2012; Abernathey and Haller, 2018; Sun et al., 2019).

Another commonly-used approach is to quantify the "eddy" contribution to ~~MHT~~ meridional HT based on the deviation of v and T from the temporal (rather than zonal) mean ~~(e.g., Cox, 1985; Jayne and Marotzke, 2002; Griffies et al., 2015; Ushakov and Ibrayev,~~ (e.g., Cox, 1985; Jayne and Marotzke, 2002; Aoki et al., 2013; Griffies et al., 2015; Ushakov and Ibrayev, 2018). Jayne and Marotzke (2002) used this formulation to assess eddy temperature fluxes and ~~MHT~~meridional HT, finding eddy temperature fluxes in energetic mid-latitude regions (Antarctic Circumpolar Current, western boundary current extensions) that are consistent with downgradient diffusivity estimates (e.g., Stammer, 1998). Volkov et al. (2008) defined the eddy contribution as the deviation from 3-month means of ~~v and T~~v and T, hence their high-frequency eddy contribution to ~~MHT~~ meridional HT was somewhat lower than the total time-varying contribution quantified by Jayne and Marotzke (2002). Yet these temporal decomposition methods may conflate the contributions of large-scale and mesoscale circulations, as gyres and long planetary

waves have temporal covariances between v and T. Moreover, the effects of stationary mesoscale features (e.g., recirculation gyres) are not included in the temporal eddy ~~MHT contributions, even though it is important to quantify these effects in order to assess coarse-resolution model parameterizations of~~ meridional HT contributions. Since spatial resolution prevents many climate models from explicitly simulating mesoscale ocean dynamics, accurate representations of the ocean depend on parameterizations (e.g., Gent and McWilliams, 1990; Eden and Greatbatch, 2008; Marshall et al., 2012) that must take into account stationary as well as transient mesoscale fluxes.

This study extends the methodology that Delman and Lee (2020) used in the North Atlantic, in order to better understand the specific contribution of mesoscale processes to meridional temperature fluxes and ~~MHT~~ meridional HT globally. Three focus areas of this study are to: (1) assess the time-mean ~~and interannual/decadal variability of mesoscale MHT relative to the overturning and large-scale circulations~~ contributions of the meridional mesoscale temperature flux (MTF), (2) compare the mesoscale ~~MHT to~~ contribution to meridional HT with other "eddy" ~~MHT~~ meridional HT diagnostics, and (3) quantify interannual/decadal variability in the MTF and determine the extent to which surface eddy kinetic energy (EKE) can be used as a proxy for ~~the variability of mesoscale temperature fluxes that contribute to MHT~~ MTF variability on these timescales. Section 2 ~~briefly~~ discusses the ocean general circulation model and methods used to quantify the components of ~~MHT~~ meridional HT. Section 3 ~~quantifies the components of MHT globally and maps the distribution of the~~ maps the mesoscale temperature flux (MTF) ~~. Section 4 compares the integrated mesoscale MHT contributions to~~ globally and discusses its contributions from stationary vs. time-varying (propagating) mesoscale dynamics. Section 4 summarizes mesoscale contributions to basin-integrated meridional HT, and compares mesoscale vs. temporally-based measures of the eddy ~~MHT~~ contribution to meridional HT. Section 5 assesses the global distribution of ~~the~~ MTF interannual and decadal variability ~~of the MTF~~ and its relationship ~~with surface EKE~~ variability to surface EKE. Section 6 discusses the key conclusions of this study and identifies areas in need of future investigation.

2 Methods

2.1 Model simulation and ~~validation~~ assessment of EKE

To quantify mesoscale temperature fluxes and contributions to ~~MHT~~ meridional HT, this analysis uses output from an eddy-permitting ocean general circulation model, the Parallel Ocean Program (POP) 2 (Smith et al., 2010). POP integrates the primitive equations with a z-depth coordinate, and is configured in a tripole grid with two north poles over Canada and Siberia. The simulation was run on the Yellowstone computing cluster (Computational and Information Systems Laboratory, 2016), with a $0.1°$ longitude grid spacing in the Mercator portion of the grid south of $\sim 28°$N, and progressively finer grid spacing approaching the two north poles. ~~The~~ In physical distance, the grid spacing is approximately 11 km near the equator, 5.5 km at $60°$S and 5–7.5 km at $60°$N. Given this spacing relative to the baroclinic deformation radius (e.g., Hallberg, 2013; Wekerle et al., 2017), it is expected that the model should at least permit mesoscale instability development equatorward of $50°$-$60°$ latitude. The model simulation has 62 depth levels with 10 meter vertical spacing in the upper 160 meters. The ocean surface is forced with Coordinated Ocean-Ice Reference Experiments version 2 (COREv2; Large and Yea-

ger, 2009) fluxes based on National Centers for Environmental Prediction reanalysis with corrections from satellite data. The
simulation was spun up during a 15-year period forced by CORE normal-year forcing (Large and Yeager, 2004), followed by
a 33-year model integration with COREv2 interannually-varying fluxes corresponding to the years 1977–2009. Our analysis
covers the 32-year period 1978–2009, the same span of time as in Delman and Lee (2020). For more details of the model
simulation see Johnson et al. (2016) and Delman et al. (2018).
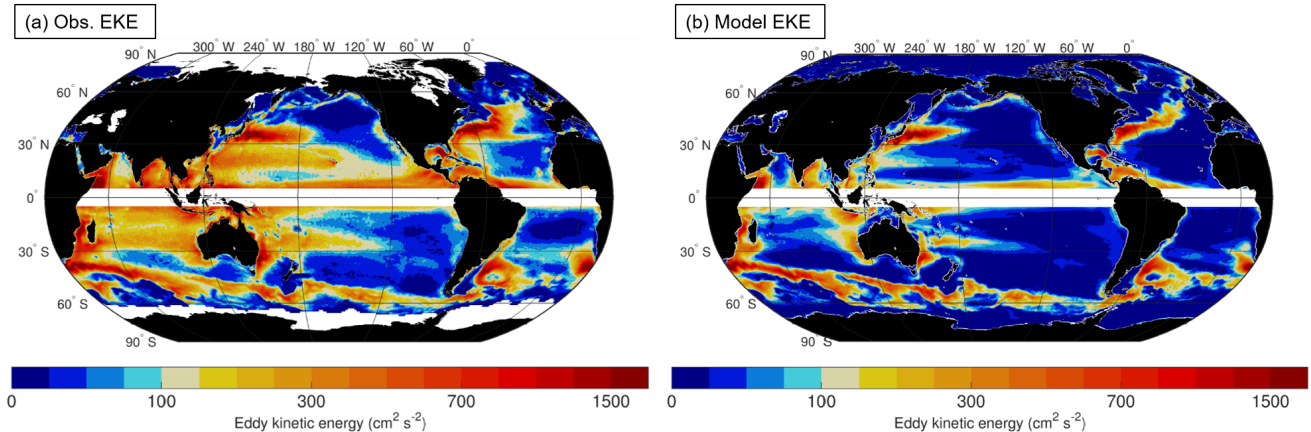
Figure 1. Time mean surface eddy kinetic energy (EKE), from (a) the Copernicus Marine Environment Monitoring Service (CMEMS) satellite-based gridded product, and (b) the POP model, with wavelengths <0.5° filtered out using a two-dimensional application of the filter in eq. (6). Time averages were computed 1993–2016 from the satellite data and the years corresponding to 1978–2009 in the model simulation. Regions within 5° latitude of the equator are masked out.

As a proxy for the model's representation of mesoscale activity globally, the model time-mean surface EKE was compared
with surface EKE from altimetry data. The altimetry dataset used is produced by Collecte Localisation Satellites (Ducet et al.,
2000) and made available through the Copernicus Marine Environment Monitoring Service (CMEMS), with data merged
from numerous altimetry missions onto a grid at 1/4° spatial and daily temporal resolution. The analysis demonstrates that
the locations and EKE levels of the most energetic regions of the ocean are well represented in the POP simulation (Figure
1). However, it is also important to note that POP underrepresents EKE in many other regions of the ocean; including the
subtropical eddy bands between 15° and 30° latitude in the North and South Pacific and South Indian Oceans, and to a lesser
extent the TIW region near the equator. ~~Therefore, our estimates of mesoscale temperature fluxes in subtropical and tropical~~
~~regions are likely to be underestimates of the true fluxes~~ This underestimation of EKE in POP persists even if a different filter
wavelength is applied to both model and altimetry datasets (e.g. 1°), and indicates a consistent low bias of mesoscale activity
in lower-energy parts of the ocean interior. One possible explanation is that the biharmonic viscosity $\nu_0 = -2.7 \times 10^{10} \text{ m}^4 \text{ s}^{-1}$
and diffusivity $\kappa_0 = -3 \times 10^9 \text{ m}^4 \text{ s}^{-1}$ values used in this model simulation are well tuned for energetic regions such as western
boundary currents, but may suppress too much mesoscale activity in the less energetic ocean interiors. However, the low bias

in time-mean EKE is not unique to this eddy-permitting model (e.g., Volkov et al., 2008, 2010). An attempt to estimate the impact of this bias on mesoscale contributions to meridional temperature fluxes and heat transport is discussed in Appendix B.

2.2 Computing the mesoscale temperature flux

110 ~~As in Delman and Lee (2020), this study decomposes meridional temperature fluxes~~ The most common method of quantifying an "eddy" flux defines the eddy meridional velocity v' and temperature T' as deviations from a time mean (e.g., $v = \bar{v} + v'$). The contributions to meridional HT are given by

$$\int \overline{vT}\,dx = \int \left(\bar{v}\bar{T} + \overline{v'T'} \right) dx \tag{1}$$

and the second term on the right-hand side is the eddy contribution. In this paper the temporal eddy flux is also referred to as
115 the "all time-varying" flux, encompassing the effects of transient/propagating phenomena at large scales as well as mesoscales. The time mean may also be implemented on shorter timescales (an example with 3-month time averages will be discussed in Section 4), or another type of time averaging (e.g., seasonal climatological averages) may be used.

In contrast, the primary focus of this manuscript uses a decomposition that targets the mesoscale by explicitly separating spatial (rather than temporal) scales. This method was used by Delman and Lee (2020), following a similar application of
120 spatial filters by Zhao et al. (2018), but with the additional separation of the overturning contribution and corrections to the filtered v and T profiles near lateral boundaries. The meridional temperature flux is decomposed into three components (over-turning, large-scale, and mesoscale) by applying spatial filters to zonal profiles of ~~meridional velocity~~ v and ~~temperature~~ T. The ~~meridional temperature transport~~ temperature flux is related to ~~MHT~~ the heat flux by a factor of ρc_ρ, where ρ is the density and c_ρ the specific heat capacity of seawater. ~~Integrated across an ocean basin~~; the heat flux integrated across a transect with
125 near-zero net volume transport is a HT. In the spatial decomposition used in this study, the meridional temperature flux ~~can be~~ at each depth level is decomposed into zonal mean and zonal deviation components

$$\int vT\,dx = \int \left(\langle v \rangle \langle T \rangle + v''T'' \right) dx \tag{2}$$

where $\langle \rangle$ indicates the zonal mean and $''$ indicates the deviation from the zonal mean. The first term on the right-hand side $\langle v \rangle \langle T \rangle$ is the overturning component of the meridional temperature flux, consistent with earlier studies (e.g., Bryan, 1982;
130 Johns et al., 2011). The overturning component, when multiplied by ρc_ρ and ~~zonally~~ vertically integrated, gives the portion of ~~MHT~~ meridional HT associated with basin-wide vertical gradients in meridional flow and temperature. The second term, variously referred to as the gyre or eddy temperature flux, contains all contributions from horizontally-varying v and T. Our method further decomposes this term into contributions from large-scale and mesoscale variations in v and T

$$v'' = v_L + v_M \tag{3}$$

$$T'' = T_L + T_M \tag{4}$$

$$v''T'' = v_L T_L + [(v_L T_M + v_M T_L) + v_M T_M] \tag{5}$$

The first term on the right-hand side is the contribution from the large-scale circulation, while the remaining three terms consti-
140   tute the mesoscale temperature flux (MTF). The cross terms $v_L T_M + v_M T_L$ are considered part of the mesoscale contribution since these fluxes would not exist without mesoscale structures. In practice, $v_L T_M$ is generally negligible compared to the other terms since zonal T profiles are red-shifted (have more large-scale structure) compared to zonal v profiles. However, $v_M T_L$ can be the largest contributor to the MTF, especially near boundaries where large-scale temperature deviations from the zonal mean are often substantial.

145   In this analysis, transects are extracted from the model output along tracks corresponding to the nearest grid faces to integer lines of latitude. In the non-Mercator portions of the grid in the Northern Hemisphere, this results in a zig-zag of the transect through the model grid, but in this way the net volume transport through each transect is conserved. The spatial filters to compute the large-scale and mesoscale v and T are applied in the ~~zonal wavenumber~~ spectral (zonal wavenumber) domain, with ~~v~~ v'' weighted by Δx (the length of each grid face along the transect) to better conserve volume transport across the
150   transect. The Fourier coefficients ~~$V(k)$ of $v\Delta x$ and T~~ $V''(k)$ of $v''\Delta x$ and T'' are filtered according to the transfer functions

$$V_L(k) = \left[0.5 + 0.5\,\mathrm{erf}\left(-s\, ln\frac{|k|}{k_0} \right) \right] \underset{\sim}{V''}(k) \tag{6}$$

$$V_M(k) = \left[0.5 + 0.5\,\mathrm{erf}\left(s\, ln\frac{|k|}{k_0} \right) \right] \underset{\sim}{V''}(k) \tag{7}$$

~~with s the steepness factor (set to 5) and k_0 the threshold wavenumberfor separating the~~ The forms of the low-pass (6) and
155   high-pass (7) filters are symmetric and contain a steepness factor s that affects the rate of signal roll-off near the cutoff wavenumber; a higher value approaches a boxcar filter with associated "ringing" effects, while a lower value avoids ringing but at the expense of cutoff precision. In filtering for ~~. Accordingly, $\lambda_0 = 1/k_0$ is the threshold wavelength for~~ large-scale and mesoscale v and T, a value of $s = 5$ was selected as an optimal balance of roll-off between the physical coordinate and spectral wavenumber domains. The sets of Fourier coefficients V_L and V_M resulting from the two filters sum to the original
160   coefficients V''. The threshold wavenumber $k_0 = 1/\lambda_0$ is the reciprocal of the threshold wavelength λ_0, which defines the scale separation between large-scale and mesoscale. Values of λ_0 in this study were set to 10° longitude poleward of 20° latitude in both hemispheres, increasing to 20° longitude within 10° of the equator. More details and a justification of these choices are given in Appendix A.

~~A zonal spatial filter was used to separate large-scale and mesoscale MHT contributions in Zhao et al. (2018); in addition to~~ ~~using a different filter, our method incorporates boundary and channel corrections (described in detail in Delman and Lee, 2020)~~ ~~to~~ To better preserve zero net volume/mass flux in the basin-integrated v_L and v_M components. ~~One aspect of note is that in~~, our method incorporates boundary and channel corrections (described in more detail in Delman and Lee, 2020). These corrections also aim to improve local representation of the large-scale/mesoscale separation near boundaries and in narrow channels. Before filtering, (1) v profiles over land areas are set to zero, and (2) a buffer is applied to temperature profiles over land areas near boundaries to avoid sharp swings in T_L. After filtering, (3) non-zero v_L and v_M that leaked onto land areas is returned to water areas, and (4) within channels bounded by bathymetry ~~, where the width of the channel is~~ that are narrower than $\lambda_0/4$, the meridional velocity ~~components~~ profiles are set to $v_L = v$ and $v_M = 0$. ~~This is because the channel is too narrow for a~~ ~~meaningful~~ Steps (1), (3), and (4) are taken in order to improve conservation of volume along the transect, while steps (2) and (3) improve the local representation of the large-scale ~~/mesoscale separation, and the basin-wide volume and mass transport~~ ~~is better conserved in the large-scale component when the channel transport is included in the large-scale circulation (e.g., the~~ ~~Gulf Stream in the Florida Strait).~~

2.3 ~~Mesoscale transition scale~~

~~Delman and Lee (2020) used $\lambda_0 = 10°$ longitude as the threshold wavelength in the North Atlantic, based on spectral analyses~~ ~~of meridional velocity and temperature at a range of latitudes. For this study, similar spectral analyses were carried out in~~ ~~the Atlantic, Indo-Pacific, and Southern ocean basins; the meridional velocity spectra are shown at various latitudes in the~~ ~~Indo-Pacific and Southern ocean basins as examples (Figure A1) . As in Delman and Lee (2020), the~~ and mesoscale ~~/large-scale~~ ~~transition and mesoscale peak wavelengths were estimated from each transect based on the logarithmically-smoothed spectral~~ ~~density profiles. The choice of $\lambda_0 = 10°$ longitude was found to be reasonable at and poleward of $20°$ latitude. Even where the~~ ~~objectively-identified transition wavelength was very different from $10°$ (e.g., $20°$S in the Indo-Pacific as shown in Fig. A1e),~~ ~~the mesoscale "bump" in the spectra clearly occurs at scales smaller than $10°$. The one exception to this pattern is at some~~ ~~tropical latitudes~~ separation. Regarding the rationale for step (4), at most latitudes mesoscale activity peaks near wavelength $\lambda_0/2$ (e.g., ~~$10°$S Indo-Pacific, Fig. A1d), where the mesoscale bump extends to scales larger than $10°$ longitude. Given this, and~~ ~~the abrupt growth of the deformation radius and typical eddy scales equatorward of $20°$ (Chelton et al., 2011), the transition~~ ~~wavelength was set to $\lambda_0 = 20°$ longitude within $10°$ of the equator, $\lambda_0 = 10°$ poleward of $20°$ latitude in both hemispheres,~~ ~~with a linear transition in λ_0 in the $10°$–$20°$ latitude range.~~

~~Zonal wavenumber spectral density of meridional velocity in POP, along latitude transects in specified basins. The black~~ ~~vertical lines and small text indicate the wavelength associated with the mesoscale transition and peak, as computed using the~~ ~~logarithmically-smoothed spectral density profile. The vertical dashed brown line indicates the wavelength λ_0 chosen for the~~ ~~mesoscalelarge-scale threshold at that latitude. The red and gray curves indicate the red noise distribution expected from lag-1~~ ~~(model grid-scale) autocorrelation and the corresponding 95% confidence bound.~~

3 ~~Global distribution of heat transport components and temperature fluxes~~

2.1 ~~Barotropic flow streamfunction~~

~~To place the global distribution of temperature fluxes in the context of the~~ Figure A1), so $\lambda_0/4$ is approximately the diameter of a typical mesoscale eddy. Channels narrower than $\lambda_0/4$ are therefore too narrow to support typical mesoscale instabilities, but transport in these channels can contribute substantially to the large-scale ~~flow field in POP, the~~ circulation (e.g., Indonesian Throughflow, Gulf Stream in the Florida Strait). Hence all of the transport in these narrow channels has been assigned to the large-scale component.

Lastly, as with the total temperature flux, the time-mean ~~cumulative zonal integral of the volume transport in each basin is shown (Figure ??).This integral is equivalent to the barotropic streamfunction, except that the circumpolar transport in the Southern Ocean is not included. The major gyre circulations are all visible in these maps; these include (1) cyclonic tropical gyres between ~0°-15° latitude in all basins except the northern Indian Ocean where the~~ MTF may contain contributions from the time-mean ~~flow is weak, (2) subtropical gyres spanning ~15°-40° latitude, except in the Southern Hemisphere where these gyres are partially connected by the Antarctic Circumpolar Current (ACC), and (3) subpolar gyres in the north Atlantic and Pacific, with the Southern Ocean dominated by the meridional drift in the ACC.~~ v and T, as well as time-varying v and T

~~POP time mean (1978–2009) cumulative zonally-integrated volume flux in the (a) Atlantic, (b) Indo-Pacific, and (c) Southern Ocean basins. This is equivalent to the barotropic streamfunction in each basin, except panel (c) does not include the Drake Passage volume transport; the latitudes south of Cape Horn are faded to indicate this.~~

$$\overline{\mathrm{MTF}} = \overline{\mathrm{MTF}_{\mathrm{stat}}} + \overline{\mathrm{MTF}_{\mathrm{vary}}} \tag{8}$$

$$\mathrm{MTF}_{\mathrm{stat}} = \overline{v_L}\,\overline{T_M} + \overline{v_M}\,\overline{T_L} + \overline{v_M}\,\overline{T_M} \tag{9}$$

$$\mathrm{MTF}_{\mathrm{vary}} = v_L' T_M' + v_M' T_L' + v_M' T_M' \tag{10}$$

2.1 ~~Spatial components of meridional heat transport~~

~~Spatial decomposition of the time mean meridional heat transport as a function of latitude (a) globally, and in the (b) Atlantic and (c) Indo-Pacific. Positive values indicate a northward heat transport.~~

When integrated zonally within ocean basins or across the global ocean, with $^{-}$ indicating a time average. The mesoscale stationary flux $\mathrm{MTF}_{\mathrm{stat}}$ is the ~~contribution of the mesoscale temperature flux(MTF) to time-mean MHT is largest at mid-latitudes, with substantial contributions in the Indo-Pacific tropics as well (Figure 7). The largest magnitude mesoscale contribution to MHT at any latitude is at 40°S, with a poleward heat transport (-0.6 PW). This exceeds the~~ contribution of the ~~large-scale MHT and nearly counters the equatorward MHT (0.8 PW) associated with the overturning at that latitude. The Northern Hemisphere mid-latitude MHT contributions are not as large; however, the mesoscale MHT contribution in the North Atlantic at 43°–45°N is almost comparable to the overturning at those latitudes (in this case both components are poleward). In the North Pacific,~~

~~the mesoscale contributes to poleward MHT at ~35°-42°N where the overturning and large-scale contributions essentially vanish. Both the Southern and Northern Hemisphere mid-latitude peaks in mesoscale MHT coincide with local minima in the~~

230 ~~magnitude of the large-scale MHT (Figure 7a).This suggests that the mesoscale plays an important part in conveying poleward MHT from the subtropical to subpolar gyres in the Northern Hemisphere, and across the subtropical edges of the Southern Ocean.Additional notable mesoscale contributions to time-mean MHT are found at the Indo-Pacific at 2°-9°N (~0.3 PW)and at 15°-11°S (~0.2 PW)~~time averages of v and T, and is often associated with boundary current recirculations and standing meanders. In this analysis the time averages are applied over the full 32 years of model output used. The mesoscale time-varying

235 flux $\mathrm{MTF_{vary}}$ is associated with rectified fluxes from transient motions (e.g., instability-generated eddies).

~~Interannual/decadal (ID) standard deviation of the spatial components of meridional heat transport (a) globally and in the (b) Atlantic and (c) Indo-Pacific basins. The ID time series of each component of MHT have been low-passed for periods longer than 14 months, with the seasonal cycle explicitly removed.~~

3 Global distribution of time-mean mesoscale temperature fluxes

240 ~~A key focus of this study is a better understanding of the interannual/decadal (ID) variability of the mesoscale contribution to MHT; accordingly the time series of the spatial components at each latitude have been temporally low-passed for periods >14 months and the seasonal cycle explicitly removed. The standard deviations of the ID filtered components (Figure 8) show that the overturning dominates MHT variability at most latitudes, but that mesoscale MHT variability can be comparable to the overturning and large-scale contributions at mid and high latitudes. Globally, the amplitude of mesoscale MHT variability at~~

245 ~~ID timescales is generally comparable to the large-scale variability poleward of 30° latitude, and comparable to the overturning variability poleward of 40° latitude in both hemispheres (Figure 8a). The largest peaks in ID mesoscale MHT variability occur at 43°–40°S, 3°–4°N, and 32°N, with the latter two peaks explained mostly by contributions from the Indo-Pacific (Figure 8c).~~

3.1 Total mesoscale temperature flux

250 ~~In order to understand the mechanisms for the time-mean and time-variable contributions of the spatial components to MHT, we consider the spatial distribution of temperature fluxes within each ocean basin. The overturning flux is by definition spatially uniform along a given transect and depth level, so we focus attention on the~~ Once computed, the distribution of the ~~large-scale temperature flux (LTF) and the MTF. One important caveat is that the LTF and MTF defined in equation (5) each~~ MTF in the global oceans highlights where mesoscale dynamics contribute most substantially to the lateral movement of heat in the

255 oceans. There is however an important caveat when inferring the physical significance of the MTF. Flux vectors consist of rotational and divergent fluxes (Marshall and Shutts, 1981); by definition, the rotational temperature (and heat) fluxes do not contribute to changes in ocean temperature or heat content and therefore are not generally of interest for climate studies. Our decomposition method is applied only in one horizontal dimension (zonally) so the divergent flux can not be neatly separated from the rotational flux except in basin integrals (where the rotational flux is negligible). However, Jayne and Marotzke (2002)

showed that rotational fluxes in mesoscale-active areas ~~also~~ typically take on mesoscale structure (i.e., they recirculate at mesoscales), while divergent meridional fluxes tend to have larger-scale structure particularly in the zonal direction.

Hence, in this study a zonal smoothing filter is applied to maps of temperature fluxes to reduce contamination from the "noise" of the rotational fluxes. This smoothing filter has the same form as the low-pass filter in equation (6)~~, but with s = 2 and~~. However, for this smoothing the threshold wavenumber k_0 ~~equal to~~ is chosen to be half the threshold wavenumber (twice the threshold wavelength) for the large-scale/mesoscale separation at that latitude. ~~Thus the mapped LTF and MTF both have large-scale structure; the~~ This larger value of the threshold wavelength is used to remove more of the rotational fluxes that occur at the mesoscale. In the smoothing filter the steepness factor s is also set to 2 (rather than 5), because the smoothing effect is more important here than the precision of the wavelength cutoff. The smoothed MTF indicates the effect of the mesoscale circulation rectified to larger scales~~, with its mesoscale structure (mostly rotational fluxes) removed~~. It is the impact of mesoscale fluxes on large-scale temperature distributions that is most relevant when quantifying the fluxes that need to be parameterized in coarse-resolution models.

~~Global maps of zonally-smoothed time-mean LTF (Figure ??) show structural patterns that generally correspond to the position of the major oceanic gyres. Within 15° of the equator, LTFs are fairly consistently towards the equator (positive south of the equator and negative to the north). These equatorward temperature fluxes associated with the horizontal circulation are in opposition to the poleward fluxes of the vertical overturning circulation at these latitudes (Figure 7), while their consistency suggests that both the western and eastern sides of the ocean basins contribute significantly to the large-scale equatorward MHT. At the latitudes of the subtropical gyres (~15°-40° latitude) the LTF generally has three distinct regions: strongly poleward in the vicinity of the western boundary, weakly equatorward in the interior western half, and weakly poleward in the eastern half of the basin. This pattern can be attributed to the asymmetry in the meridional flow; the poleward flow is concentrated very close to the western boundary (Figure ??), while the temperature profile in the upper ocean (warmer in the west, cooler in the east) changes more gradually. Hence the equatorward temperature flux results from equatorward (generally Sverdrup flow) in the warmer part of the basin. Nonetheless, the strongest contribution from the large-scale subtropical gyre is poleward, at the western boundary. This picture becomes more complex in the Northern Hemisphere subpolar gyres (Fig. ??a,b) and the Southern Ocean (Fig. ??c). In the subpolar gyres, poleward temperature fluxes are substantial near both western and eastern boundaries. In the Southern Ocean, poleward (negative) temperature fluxes are most substantial where there are meridional excursions in the ACC, such as east of South America (60°-30°W), south of Australia (100°-160°E), and before the entrance to Drake Passage (240°-280°E).~~

Maps of zonally-smoothed time-mean MTF (Figure 2) show that the mesoscale contributions to ~~MHT~~ meridional HT are generally concentrated near the western boundary~~, even more so than LTF contributions~~. Even in the tropics, MTF contributions are mostly confined to the western boundaries, with the exception of the TIW band in the north-central equatorial Pacific, and to a lesser extent in the eddy-rich region south of Indonesia. ~~As Figure 7 implies, the impact of both LTF and MTF contributions to MHT~~ The impact of MTF contributions is generally to flux heat equatorward in the tropics, and poleward at higher latitudes. ~~Consistent with this, the time-mean meridional MTF in a given location usually has the same sign as the LTF, indicating that the mesoscale reinforces or intensifies the impact of the time-mean large-scale circulation.~~ However, there are ~~a few~~

Figure 2. POP time-mean northward temperature flux associated with the mesoscale flow (MTF), in units of terawatts per kilometer (TW km⁻¹), zonally low-passed using a wavelength equal to twice the large-scale/mesoscale threshold wavelength at each latitude. Fluxes shown in the (a) Atlantic, (b) Indo-Pacific, and (c) Southern Ocean basins.

295 notable exceptions where the mesoscale counteracts the time-mean LTF. The western boundary of the southern Indian Ocean has a poleward LTF but an equatorward MTF, implying compensation of the large-scale gyre heat transport by mesoscale circulations (MTF fluxes heat equatorward even at mid-latitudes, most notably in the western boundary currents of the South Indian (Agulhas Current) and South Pacific (East Australian Current) near 30°S (Figure 2b). A similar compensation is evident in the East Australian Current near southeast Australia, and in the Equatorward MTF is also apparent in the Labrador Sea at

300 the western edge of the North Atlantic subpolar gyre (Figure 2a). We note that the significant low EKE bias in many ocean interiors (Figure 1) implies that MTF may be underestimated in interior regions, especially at low latitudes. An assessment of the potential impact of this bias using composite averages is discussed in Appendix B.

3.2   Contributions of stationary versus time-varying mesoscale structure

As with the total temperature flux, the time-mean MTF may contain contributions from the time-mean v and T, as well as
305   time-varying v and T

$$\overline{\mathrm{MTF}} = \overline{\mathrm{MTF}_{\mathrm{stat}}} + \overline{\mathrm{MTF}_{\mathrm{vary}}}$$

$$\overline{\mathrm{MTF}_{\mathrm{stat}}} = \overline{v_L}\,\overline{T_M} + \overline{v_M}\,\overline{T_L} + \overline{v_M}\,\overline{T_M}$$

310   $$\overline{\mathrm{MTF}_{\mathrm{vary}}} = \overline{v'_L T'_M} + \overline{v'_M T'_L} + \overline{v'_M T'_M}$$

with $\overline{}$ indicating a time average. The stationary part of the contribution
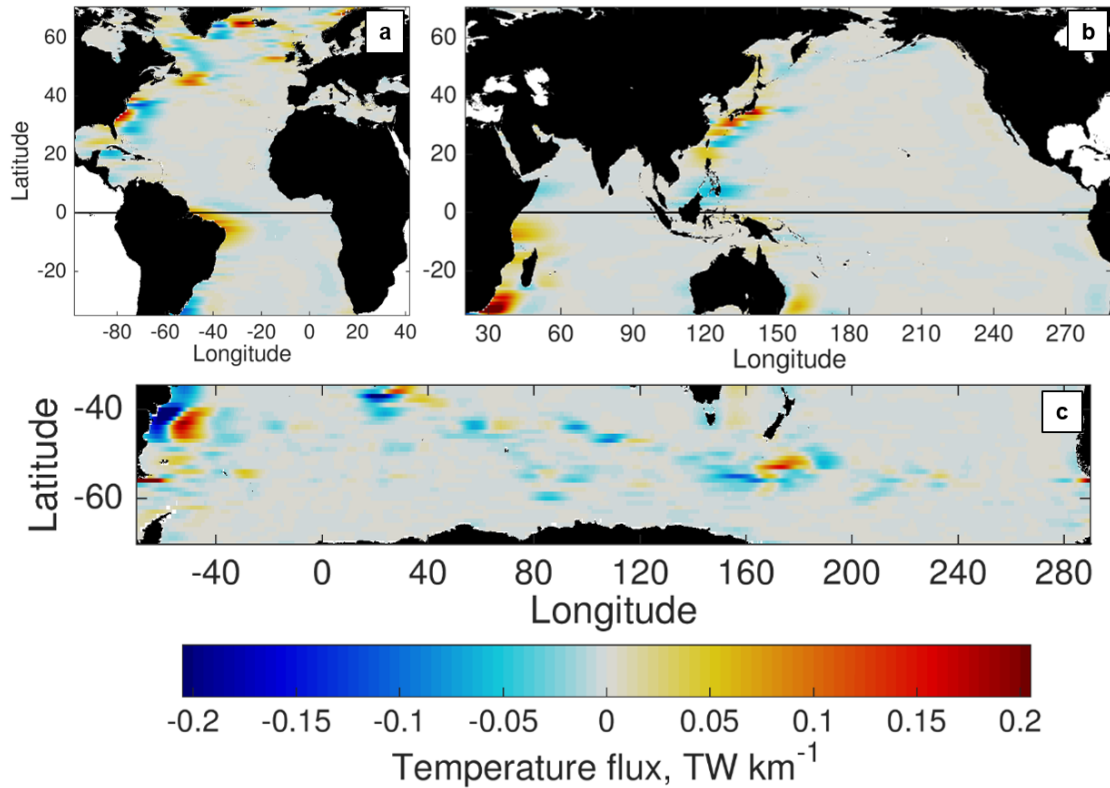
Figure 3. POP time mean meridional temperature flux associated with the stationary mesoscale flow only ($\overline{\mathrm{MTF}_{\mathrm{stat}}}$), zonally low-passed. Fluxes shown in the (a) Atlantic, (b) Indo-Pacific, and (c) Southern Ocean basins.

The stationary part of the MTF, excluded from temporal definitions of the eddy flux, comprises a substantial portion of the total MTF globally (Figure 3). At lower latitudes (equatorward of 40° in both hemispheres), contributions from $\mathrm{MTF_{stat}}$ ~~can be explained in terms of time averages of the v and T components, while the time-varying part $\mathrm{MTF_{vary}}$ is associated with rectified fluxes from transient motions (e.g., instability-generated eddies)~~ are overwhelmingly concentrated near the western boundaries of ocean basins. In the Southern Ocean, stationary contributions are found near meridional excursions in the Antarctic Circumpolar Current (ACC) at the Brazil-Malvinas Confluence and south of New Zealand. In the North Atlantic, $\mathrm{MTF_{stat}}$ contributions are found in the Labrador Sea, Irminger Sea (between Greenland and Iceland), and near the coasts of the British Isles and Scandinavia. Because of the importance of the flow and temperature structure at mesoscales, all of these regions are areas where temperature fluxes are likely to be incorrectly represented in coarse-resolution climate models, unless these fluxes are properly parameterized.
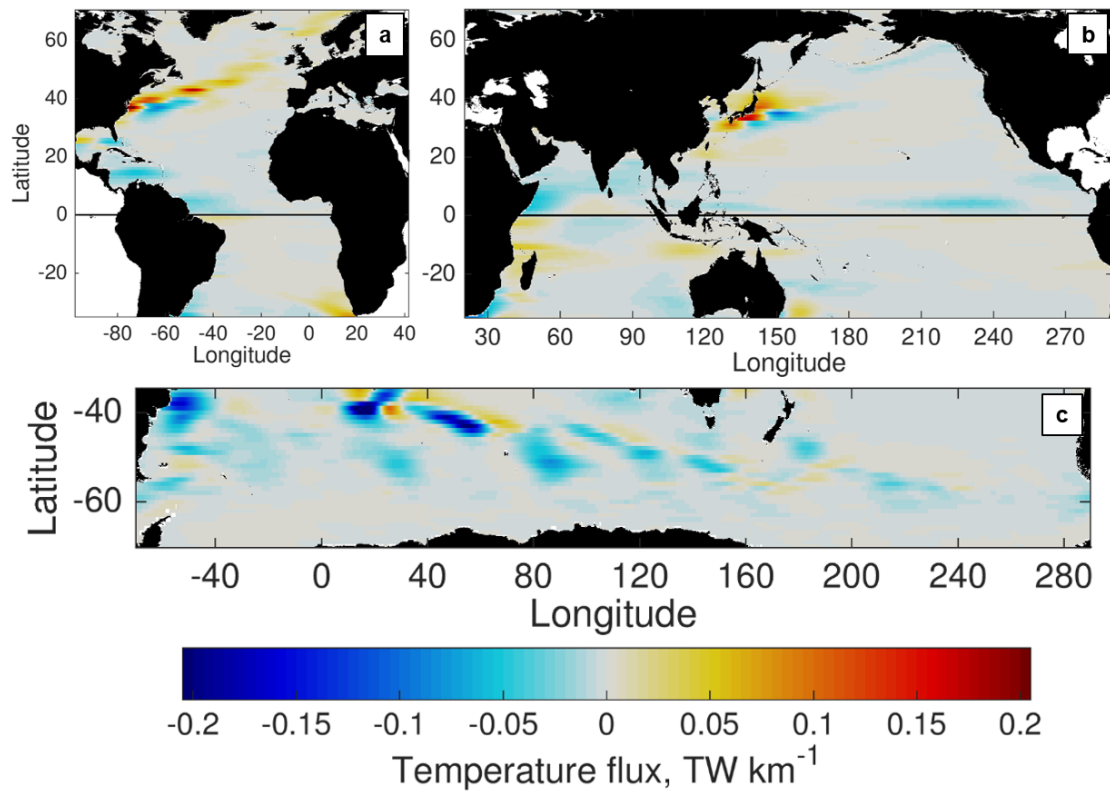
Figure 4. ~~Left column: Decomposition of the time-mean~~ POP time mean meridional ~~velocity at 95 m depth into large-scale v_L and mesoscale v_M in~~ temperature flux associated with the ~~Indo-Pacific basin~~ time-varying mesoscale flow only ($\overline{\mathrm{MTF_{vary}}}$), ~~along latitude transects specified at left~~ zonally low-passed. ~~Center column: Same but for~~ Fluxes shown in the ~~decomposition of time-mean temperature into T_L and T_M. Right column: The time-mean full-depth mesoscale temperature flux~~ (a) Atlantic, ~~cumulatively integrated from west to east~~ (b) Indo-Pacific, ~~showing the total $\overline{\mathrm{MTF}}$, $\overline{\mathrm{MTF_{stat}}}$, and $\overline{\mathrm{MTF_{vary}}}$~~ (c) Southern Ocean basins.

The time-varying $\mathrm{MTF_{vary}}$ is closer to the temporal eddy flux $v'T'$, but our definition excludes larger-scale temporal variability. As might be expected, $\mathrm{MTF_{vary}}$ contributions are found mostly in regions where the model also has relatively high EKE (Figure 4): the Gulf Stream and North Atlantic Current, the Kuroshio Extension, the north equatorial Pacific, South Equatorial Current in the Indian Ocean, and the ACC. Many areas that have large $\mathrm{MTF_{stat}}$ also have large $\mathrm{MTF_{vary}}$, including

325   most western boundary regions and the ACC. However, ocean interior regions such as the North Atlantic Current and the north equatorial Pacific TIW area have large $\mathrm{MTF_{vary}}$ without substantial $\mathrm{MTF_{stat}}$ contributions, indicating that the flows driving these fluxes are both mesoscale and transient. In the Southern Ocean, the Agulhas Return Current (near 40°S, 0–60°E) and the lee of the Kerguelen Plateau (near 50°S, 80–90°E) are areas where the MTF is dominated by the transient rather than the stationary contribution. The distribution of $\mathrm{MTF_{vary}}$ in Figure 4 resembles the divergent component of the temporal

330   eddy flux (Jayne and Marotzke, 2002; Aoki et al., 2013), but with some distinctions; for instance, the near-equatorial fluxes are not as high-amplitude in Figure 4. This may be due to the dominance of long planetary waves at these latitudes, which are time-varying phenomena (temporal "eddy") but our analysis considers to be large scale, not mesoscale.
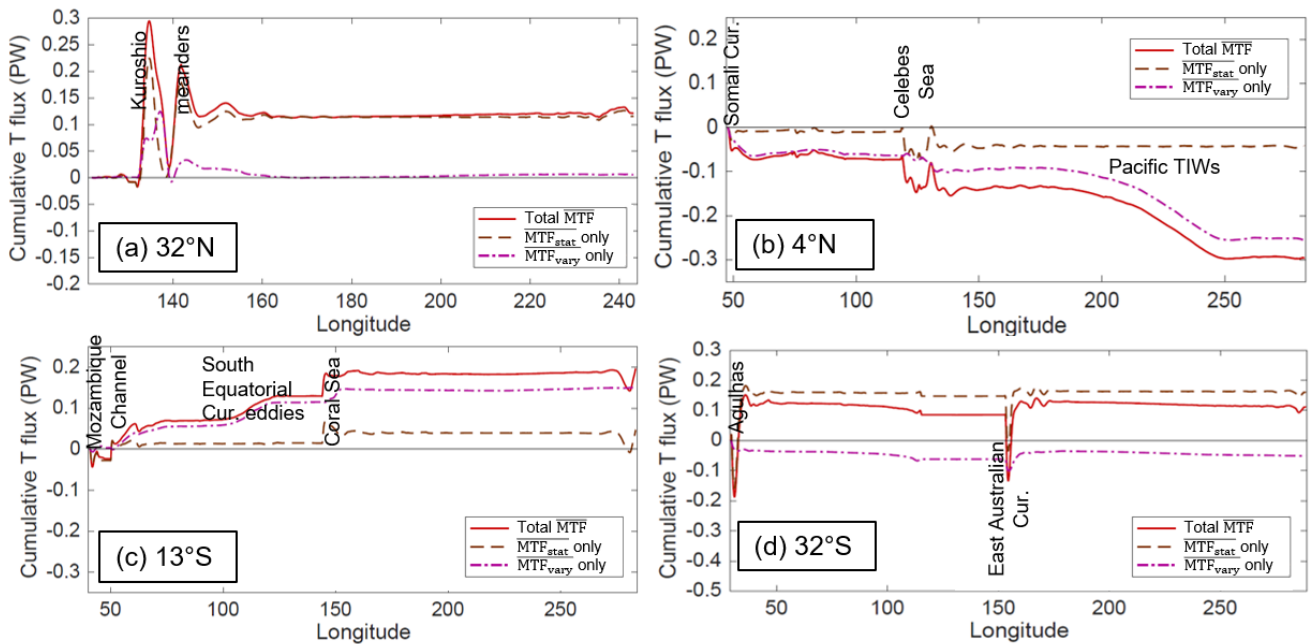
Figure 5. The time mean full-depth mesoscale temperature flux in the Indo-Pacific basin, cumulatively integrated from west to east, showing the total MTF, the part of the MTF attributed to time mean v and T components only $\overline{\mathrm{MTF_{stat}}}$, and the part attributed to time-varying v and T components that have a rectified contribution to time-mean MTF $\overline{\mathrm{MTF_{vary}}}$. Transects are shown for latitudes (a) 32°N, (b) 4°N, (c) 13°S, and (d) 32°S.
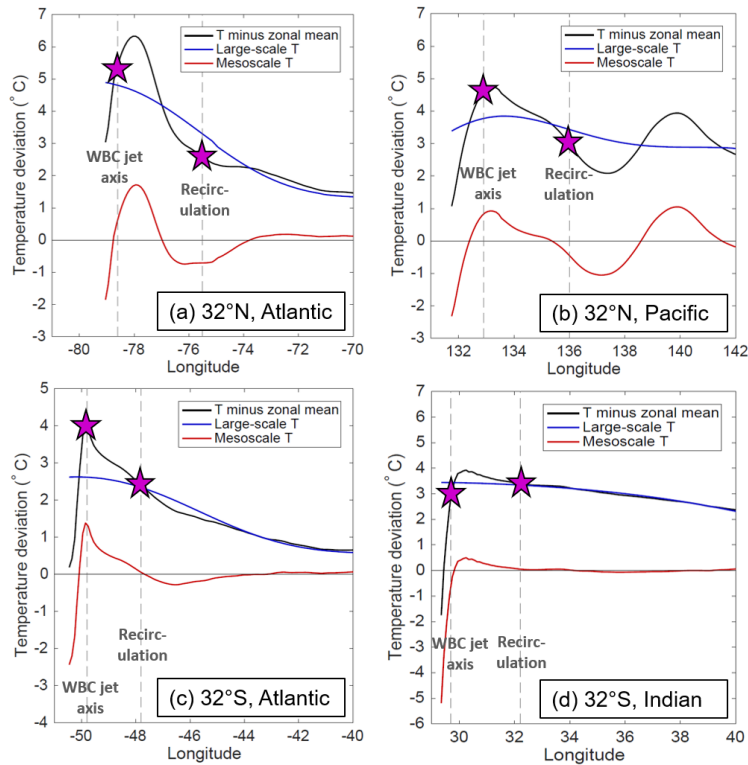
~~Temperature profiles at 95 m depth near the western boundary in the specified latitude and basin. The vertical gray dashed lines indicate the locations of peak velocities associated with the poleward western boundary current (WBC) jet, and the equatorward recirculation. The difference in temperature between these two locations (magenta stars) provides an indication of the mesoscale temperature flux from the jet and recirculation.~~

Figure 6. Time mean temperature profiles at 95 m depth near the western boundary in the specified latitude and basin. The vertical gray dashed lines indicate the locations of peak velocities associated with the poleward western boundary current (WBC) jet, and the equatorward recirculation. The difference in temperature between these two locations (magenta stars) provides an indication of the mesoscale temperature flux from the jet and recirculation.

~~Figure ?? considers the contributions from stationary features relative to the time-varying flux at certain latitudes in the Indo-Pacific where the MTF is relatively large (Figure 7c). All of the mid-latitude and tropical transects in Figure ?? have~~ 335 ~~western boundary currents (WBCs). These currents contribute to a peak in v_L near the coast, as well as an intensified boundary current jet and flanking recirculation just to the east that is shown in v_M (Figure ??, left column). These jet-recirculation pairs are mesoscale structures, since the core of the jet and the recirculation flow in opposite directions and are separated by only 2°-3° longitude. By integrating the MTF across each transect from west to east (Figure ??, right column) , it can be seen that the~~ Some insight can be gained about the contributions of stationary vs. time-varying contributions to meridional

340   HT by considering the cumulative zonal integral of each MTF component. Figure 5 shows this analysis for latitudes in the Indo-Pacific with relatively large MTF. It can be seen that stationary MTF contributions are typically associated with western boundaries ~~: namely in~~ (the western Pacific at 32°N, 4°N, and 13°S, and the western Indian at 32°S~~. Furthermore, while~~), and that the zonally-integrated MTF_{stat} contribution is much larger than MTF_{vary} at the mid-latitude locations. Time-varying MTF_{vary} contributions are more substantial at the low-latitude locations (4°N and 13°S~~have larger contributions

345 from time-varying mesoscale dynamics MTF_{vary}, it is the stationary structures MTF_{stat} that contribute most to MTF at the mid-latitude transects~~), and can be found both near the basin boundaries (Somali Current and Mozambique Channel/Mascarene Basin respectively) and in the ocean interiors (Pacific TIWs and South Equatorial Current eddies respectively).

  ~~If~~ Since stationary mesoscale contributions to ~~MHT are substantial , especially at mid-latitudes, then~~ meridional HT are substantial (Figure 5), it is important to understand the velocity and temperature structure that contributes to the flux. ~~The

350 stationary MTFs~~ For example, the MTF_{stat} contributions near mid-latitude western boundaries are driven by a temperature difference between the poleward WBC jet and the equatorward recirculation (Figure 6). In the Gulf Stream, Kuroshio, and Brazil Current poleward of ∼30° latitude, the poleward jet is associated with a local maximum in temperature due to the advection of waters from lower latitudes (Figure 6a-c). As a result, the water in the jet is warmer than the water in the recirculation, and the net MTF is poleward (Figure 2a-b). In contrast, the jet of the Agulhas is coincident with a steep gradient in temperature

355 without a local maximum in temperature (Figure 6d); hence the water in the jet is cooler than in the recirculation and the net MTF is equatorward. The sign of the MTF associated with WBCs therefore depends on whether the local temperature profile is determined more by the temperature advection of the WBC jet (poleward MTF), or the frontal gradient that the WBC is aligned with (equatorward MTF). Most WBCs have both characteristics, but the degree to which one is dominant can be the difference between a stationary flux that is 0.12 PW poleward (Figure ~~??~~5a) and 0.16 PW equatorward (Figure ~~??~~5d).

360 **4**   ~~Difference between spatial and temporal flux decompositions~~**Contributions to zonally-integrated meridional HT**

~~By targeting mesoscale spatial scales, our approach differs from methods that quantify "eddy" contributions to MHT based on temporal deviations in v and T. The temporal decomposition defines the "eddy" v' and T' as deviations from the time mean (e. g., $v = \bar{v} + v'$), and the contributions to MHT are given by~~

4.1   **Spatial decomposition of meridional HT**

365 ~~and the second term on the right-hand side is~~ When integrated zonally across the global ocean or within ocean basins, the contribution of the mesoscale temperature flux (MTF) to time-mean meridional HT is largest at mid-latitudes, with substantial contributions in the Indo-Pacific tropics as well (Figure 7). The largest magnitude mesoscale contribution to meridional HT at any latitude is at 40°S, with a poleward heat transport (-0.6 PW) powered by strong MTF in the ~~eddy contribution. Most commonly, the time mean is computed over the entire period of record (which in this study would be the~~ Brazil-Malvinas

370 Confluence and Agulhas Return Current regions (Figure 2). This exceeds the contribution of the large-scale meridional HT and nearly counters the equatorward meridional HT (+0.8 PW) associated with the overturning at that latitude. The Northern

$$\int \overline{vT}\, dx = \int \left(\overline{v}\,\overline{T} + \overline{v'T'} \right) dx$$
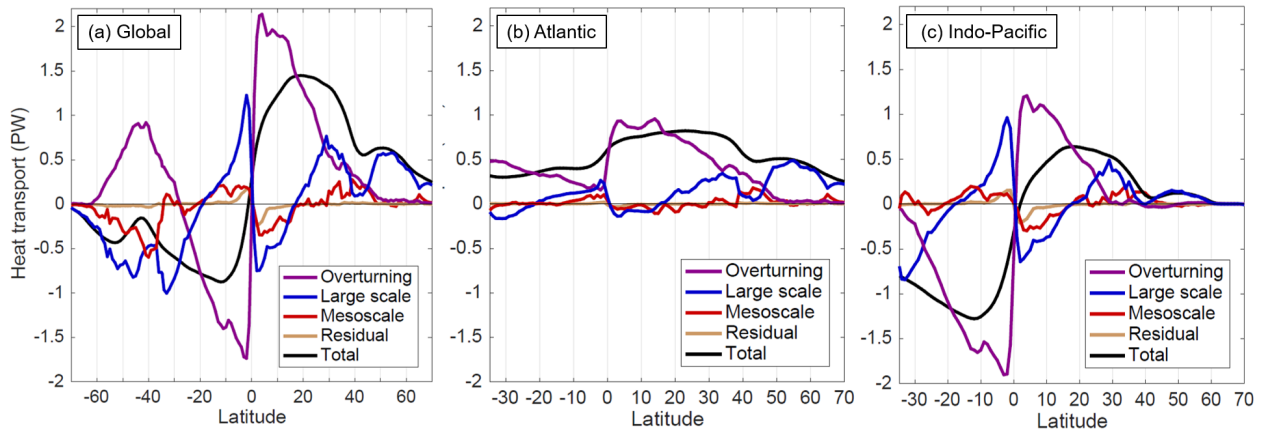
Figure 7. Spatial decomposition of the time mean meridional heat transport as a function of latitude (a) globally, and in the (b) Atlantic and (c) Indo-Pacific. Positive values indicate a northward heat transport. The residual consists of the effect of high-frequency co-variations in v and T (timescales <5 days) archived as fluxes in POP, which could not be spatially decomposed into individual v and T profiles.

Hemisphere mid-latitude meridional HT contributions are not as large; however, the mesoscale meridional HT contribution in the North Atlantic at 43°–45°N is almost comparable to the overturning at those latitudes (in this case both components are poleward). In the North Pacific, the mesoscale contributes to poleward meridional HT at ~35°–42°N where the overturning
375   and large-scale contributions essentially vanish. Both the Southern and Northern Hemisphere mid-latitude peaks in mesoscale meridional HT coincide with local minima in the magnitude of the large-scale meridional HT (Figure 7a). This suggests that the mesoscale plays an important part in conveying poleward meridional HT from the subtropical to subpolar gyres in the Northern Hemisphere, and across the subtropical edges of the Southern Ocean. Additional notable mesoscale contributions to time-mean meridional HT are found at the Indo-Pacific at 2°-9°N (-0.3 PW) and at 15°-11°S (+0.2 PW).
380   A key focus of this study is a better understanding of the interannual/decadal (ID) variability of the mesoscale contribution to meridional HT; accordingly the time series of the spatial components at each latitude have been temporally low-passed for periods >14 months and the seasonal cycle explicitly removed. The standard deviations of the ID filtered components (Figure 8) show that the overturning dominates meridional HT variability at most latitudes. This is not surprising since the overturning component of meridional HT highlights the effect of temperature differences between the shallow and deep ocean, and at
385   lower latitudes these vertical differences are much larger than zonal temperature differences across ocean basins. However, mesoscale contributions to meridional HT variability can be comparable to the overturning and large-scale contributions at mid and high latitudes. Globally, the amplitude of mesoscale meridional HT variability at ID timescales is generally comparable to the large-scale variability poleward of 30° latitude, and comparable to the overturning variability poleward of 40° latitude in
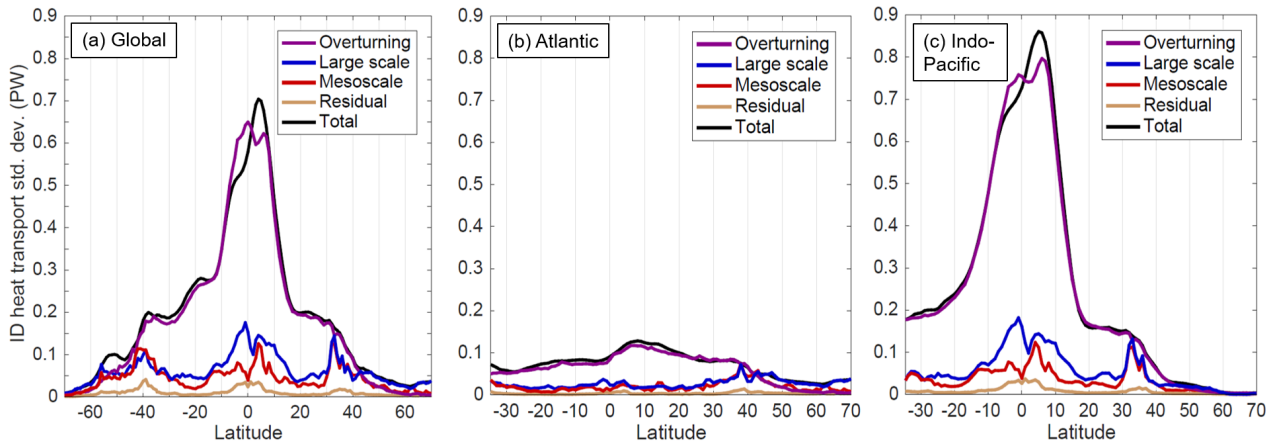
Figure 8. Interannual/decadal (ID) standard deviation of the spatial components of meridional heat transport (a) globally and in the (b) Atlantic and (c) Indo-Pacific basins. The ID time series of each component of meridional HT have been low-passed for periods longer than 14 months, with the seasonal cycle explicitly removed.

both hemispheres (Figure 8a). The largest peaks in ID mesoscale meridional HT variability occur at 43°–40°S, 3°–4°N, and

390   32 ~~years of model output). An alternative approach (Volkov et al., 2008) computes the eddy term as the deviation from 3-month time means, so that the eddy contribution includes intraseasonal variations, but not seasonal or interannual variations. In this study, the~~ °N, with the latter two peaks explained mostly by contributions from the Indo-Pacific (Figure 8c). These latitudes correspond to the high EKE regions associated with the Agulhas Return Current, Pacific TIWs, and Kuroshio respectively, implying that the very active mesoscale dynamics and interannual variability in these areas result in large MTF variability on

395   ID timescales as well.

The mesoscale contribution to ~~MHT~~ meridional HT using our method ~~is compared to both~~ can also be compared to two definitions of the ~~temporal eddy contribution , which are called the "~~eddy contribution based on a temporal decomposition. The "all time-varying" ~~and~~ contribution consists of the residual eddy term on the right-hand side of eq. (1) when the contribution from the 32-year time averages of v and T are removed. The "high frequency" ~~components respectively.~~

400   ~~Comparison of various "eddy" formulations of the meridional heat transport as a function of latitude (a) globally, and in the (b) Atlantic and (c) Indo-Pacific. The three formulations are the mesoscale component, the time-varying component $v'T'$, and the high frequency component computed from v' and T' on timescales shorter than 3 months.~~

~~Regarding contributions to the time-mean MHT, neither the~~ contribution, following (Volkov et al., 2008), is the residual eddy term when time averages of v and T in each 3-month period are removed (i.e., consists of variability at timescales

405   shorter than ~3 months). When zonally-integrated globally and across ocean basins, neither the all time-varying nor high frequency components are uniformly consistent with the mesoscale contribution (Figure 9). Generally, the mesoscale ~~MHT~~ meridional HT is closer to the high frequency contribution at low latitudes, and closer to the all time-varying contribution
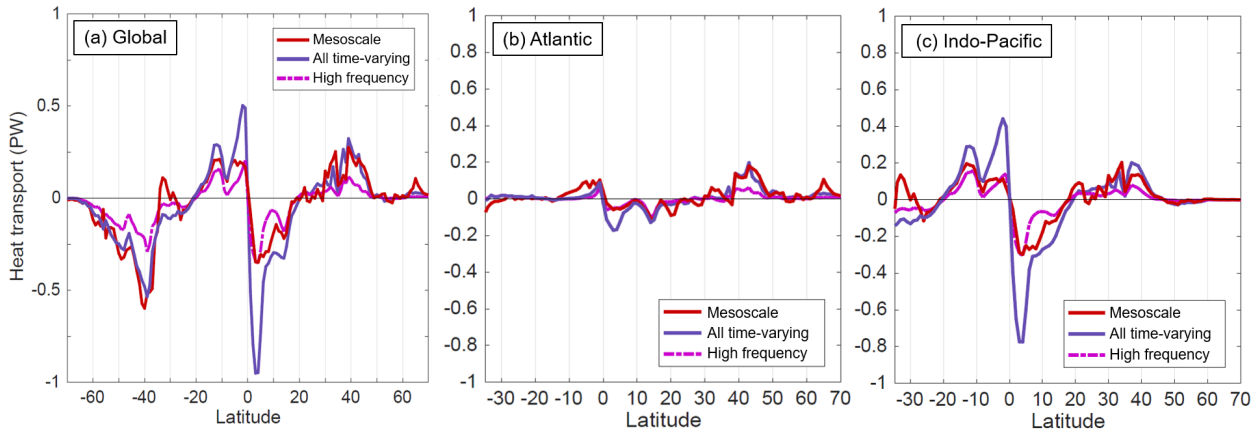
Figure 9. Comparison of various "eddy" formulations of the meridional heat transport as a function of latitude (a) globally, and in the (b) Atlantic and (c) Indo-Pacific. The three formulations are the mesoscale component computed based on eq. (5), the all time-varying component $\overline{v'T'}$, and the high frequency component computed from v' and T' on timescales shorter than 3 months.

at mid latitudes. One possible inference from this is that mesoscale dynamics tend to have consistently high frequencies in the tropics (where planetary wave and eddy propagation speeds are higher), while mesoscale dynamics at higher latitudes tend to propagate more slowly and take on lower frequencies. The difference between all time-varying and mesoscale ~~MHT~~ meridional HT close to the equator may also be associated with the impact of long Kelvin and Rossby waves, which are ~~both large-scale and time variable. Hence~~ time-varying ~~and high frequency MHT may include the impacts~~ with frequencies ranging from intraseasonal to interannual, but with spatial wavelengths comparable to the size of an entire ocean basin (e.g. Boulanger and Menkès, 1999; McPhaden and Yu, 1999). Hence the temporal eddy fluxes conflate the contributions of large-scale ~~variability that have very different dynamics from mesoscale eddies.~~ planetary wave activity and mesoscale eddy activity. In contrast, the mesoscale component isolates the contributions to meridional HT from fluxes that are not expected to be well represented in coarse-resolution climate models.

A comparison of the standard deviation associated with the ID time series of the three components (Figure 10) shows that all three components have spikes in temporal variability in the mid-latitudes and near the equator. As with the contributions to time-mean ~~MHT~~ meridional HT, the ID variability of the mesoscale contribution more closely resembles the time-varying contribution at mid-latitudes. In the tropics, the ID variability of the mesoscale does not resemble either component; in the tropical Indo-Pacific the high frequency and time-varying standard deviations are both larger than the mesoscale, implying substantial contributions from large-scale ID variability.
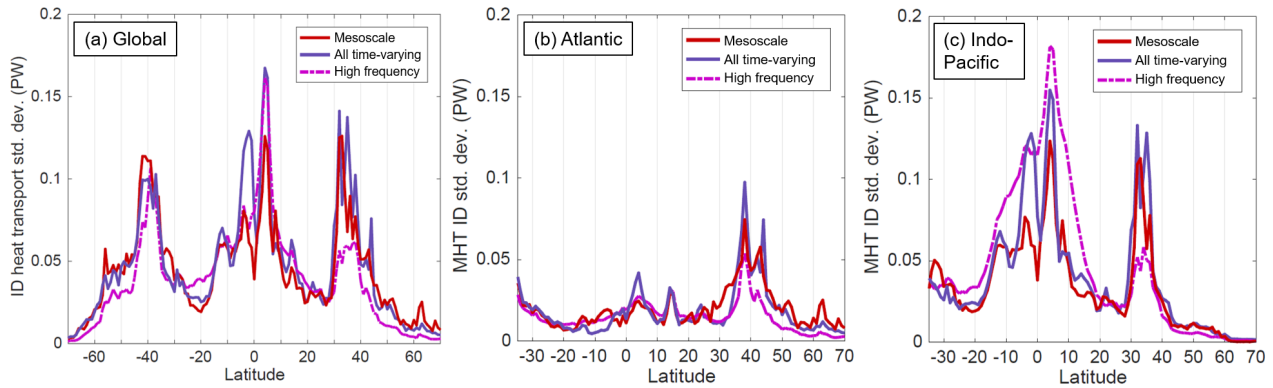
Figure 10. Interannual/decadal (ID) standard deviation of the spatial and temporal "eddy" formulations (a) globally and in the (b) Atlantic and (c) Indo-Pacific basins.

5 Mesoscale interannual/decadal variability

5.1 Locations of substantial mesoscale contributions

Mesoscale dynamics influence not only the time-mean ~~MHT~~ meridional HT but also its variability on ID timescales (Figure 8), motivating a study of the regions where the mesoscale contributions to ID temperature flux variability are greatest. As with the time-mean MTF, the interannual and decadal variability of the MTF is mostly concentrated near western boundaries, the ACC, and the north equatorial Pacific and southern tropical Indian oceans (Figure 11). High levels of ID variability of the MTF also generally coincide with regions of high EKE in the POP model simulation (Figure 1b). Notably, the subtropical eddy bands in the Pacific and Indian Oceans seem to have a negligible impact on MTF ID variability. The POP model does underestimate EKE in these eddy bands relative to altimetry (Figure 1), but it still shows these bands as regions of elevated EKE; in contrast there is almost no elevation in ID MTF variability associated with these eddy bands. This indicates that mesoscale fluxes are not ~~be~~ particularly efficient at moving heat meridionally in subtropical eddy bands, at least in the POP simulation.

~~Time series of spatial components of MHT variability in the Southern Ocean across (a)-(b) 56°S and (c)-(d) 42°S, with time means removed. The top row shows all spatial components; the bottom row has the overturning component removed. The dashed vertical red lines in (b) and (d) indicate episodes where mesoscale MHT drives variations in the total non-overturning MHT.~~

~~Time series of spatial components of MHT variability in the Indo-Pacific basin across (a)-(b) 13°S, (c)-(d) 4°N, and (e)-(f) 32°N, with time means removed. The top row shows all spatial components; the bottom row has the overturning component removed. The dashed vertical red lines in (b) and (d) indicate episodes where mesoscale MHT drives variations in the total non-overturning MHT. In panel (d) some major El Niño (El N) and La Niña (La N) events coincident with mesoscale extrema are also annotated.~~
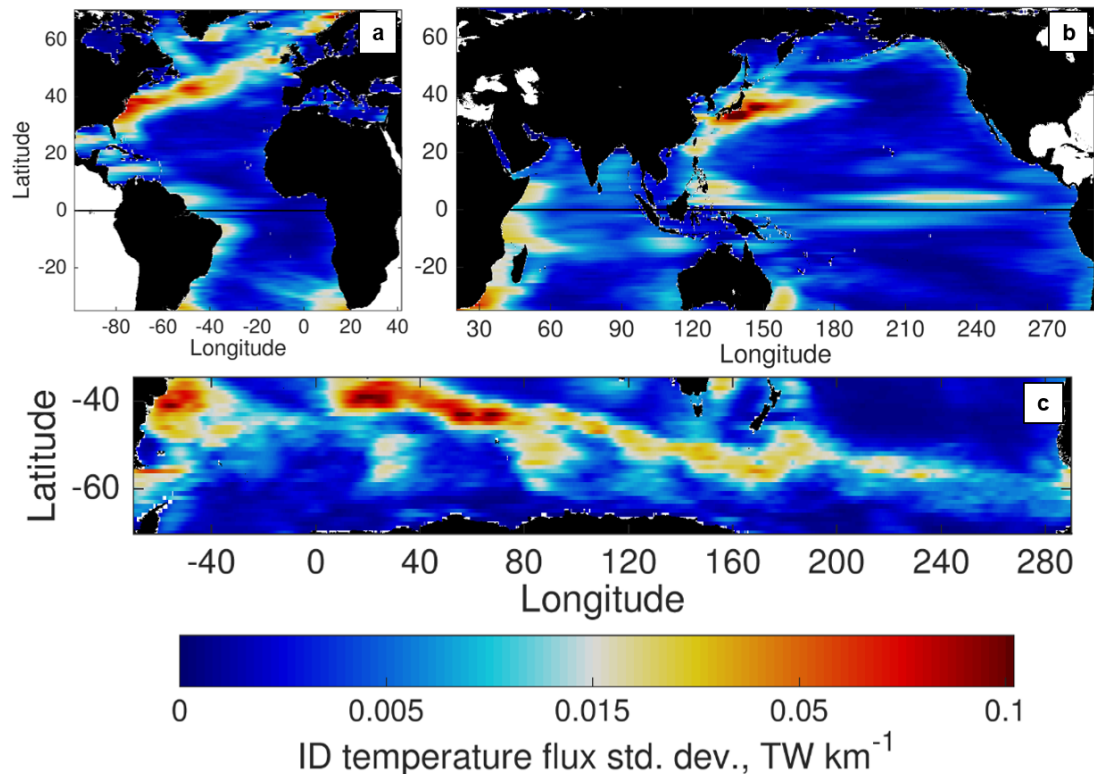
Figure 11. Standard deviation ~~on ID timescales~~ of the ~~interannually-varying meridional temperature flux associated with the mesoscale flow~~MTF, zonally smoothed ~~using the same smoothing filter as in Figures 2–4~~. The ~~"interannually-varying"~~ flux is ~~ID time series of MTF have been~~ low-passed for periods >14 months prior to the computation of the standard deviation. Fluxes ~~are~~ shown in the (a) Atlantic, (b) Indo-Pacific, and (c) Southern Ocean basins.

~~Time series at specific latitudes can provide context for the contributions of MTFs relative to overturning and large-scale temperature fluxes. In the Southern Ocean, peaks in basin-integrated MTF ID variability occur at 56°S and 42°S (Figure 8a), but the role of the MTF is very different. At 56°S, the large-scale temperature flux is the driving component of ID MHT variability, with the mesoscale compensating (counteracting) the large-scale contributions to some extent (Figure ??a-b). One exception is the 1995–96 episode, when a positive (northward) mesoscale MHT anomaly pushes the total MHT at 56°S despite a negative large-scale MHT anomaly. In contrast, at 42°S numerous extrema in the total MHT anomaly can be attributed to the mesoscale component (Figure ??d). This latitude is near the largest mesoscale contribution to time-mean MHT as well (at 40°S), indicating the impact of mesoscale dynamics on both the MHT steady state and ID variations in the Southern Hemisphere mid-latitudes.~~

~~Despite the overall dominance of the overturning circulation in MHT variability at low latitudes, mesoscale contributions are still substantial at certain latitudes. Most of these contributions are in the Indo-Pacific, where local maxima in mesoscale MHT~~

445

450
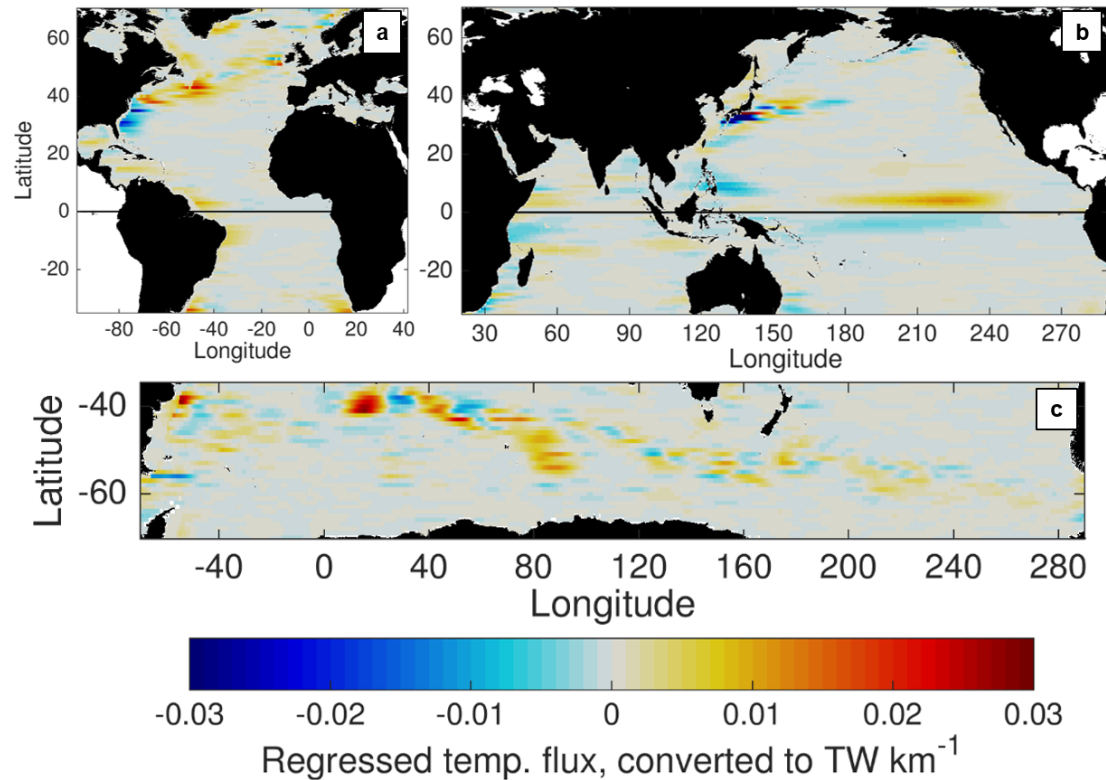
Figure 12. Local (zonally-smoothed) mesoscale temperature flux R_{MTF} that contributes to ~~the~~ 1 standard deviation of total ~~MHT~~ meridional HT variability on ID timescales, computed by linear regression at each latitude and basin. Positive values indicate that the MTF is positively correlated with (contributes to) total ID ~~MHT~~ meridional HT variability; negative values indicate that the MTF is negatively correlated with (compensates) total ID ~~MHT~~ meridional HT variability.

455 ~~variability are located at 13°S, 4°S, and 4°N (Figures 8c, 11). With the overturning removed, the mesoscale contributions to ID MHT variability are quite apparent in the time series at 13°S and 4°N (Figures 13b,d). At 4°N many of these mesoscale extrema coincide with El Niño or La Niña events, likely due to the TIW activity across much of the Pacific at this latitude. The MTF variability is larger in the Pacific at 4°N than at 4°S (Figure 11), consistent with the larger EKE north of the equator (Figure 1). In contrast, the ID MTF variability in the mid-latitude Pacific at 32°N largely acts to compensate the large-scale~~

460 ~~fluxes, leaving overturning MHT to drive total MHT variability (Figure 13e,f).~~

~~Time series of spatial components of MHT variability in the Atlantic Ocean across (a)-(b) 43°N and (c)-(d) 63°N, with the time means removed. The top row shows all spatial components; the bottom row has the overturning component removed. The dashed vertical red lines in (b) and (d) indicate episodes where mesoscale MHT drives variations in the total non-overturning MHT.~~

465 ~~One more area of substantial ID MHT variability is in the North Atlantic, where large MTF variability is found extending across the ocean from the Gulf Stream near the southeast U.S. coast, to the North Atlantic Current near the British Isles (Figure 11). At 43°N in the Atlantic, where the amplitude of ID MHT variability is nearly equal between the three components, a number of total MHT extrema can be attributed to the mesoscale component (Figure ??b). Elevated variability is also found further north near the coasts of Greenland and Norway (Figure 11). At 63°N the overturning component no longer influences~~

470 ~~MHT variability substantially, but large-scale and mesoscale fluxes both contribute to the total MHT time series (Figure ??d).~~

Another way to assess the contributions of MTF variability to basin-integrated ~~MHT~~ meridional HT on ID timescales is to compute a linear regression or correlation between (1) the time series of ~~MHT~~ meridional HT integrated across the basin at each latitude and (2) the local zonally-smoothed MTF time series along the transect. This regression-based flux contribution can be expressed as

$$R_{\mathrm{MTF}} = R_{\frac{\mathrm{loc}}{\mathrm{tot}}}\sigma_{\mathrm{tot}} = C(\mathrm{loc}, \mathrm{tot})\sigma_{\mathrm{loc}} \tag{11}$$

475

where $R_{\frac{\mathrm{loc}}{\mathrm{tot}}}$ is the linear regression coefficient of the local MTF given the time series of the total basin-integrated temperature flux, σ_{loc} and σ_{tot} are the standard deviations of the local and total basin-integrated time series respectively, and $C(\mathrm{loc}, \mathrm{tot})$ is the correlation coefficient of the local and total basin-integrated time series. The regression flux contribution R_{MTF} is the local temperature flux that would be expected to contribute to a basin-integrated value of 1 standard deviation above the mean;

480 positive (negative) values of R_{MTF} indicate a positive (negative) correlation of the two time series. R_{MTF} can be expressed in units of temperature flux or heat flux, and the latter are used here. A similar analysis was shown in Figures 7-8 of Delman and Lee (2020) in profiles of longitude-depth, but ~~MTFs are mostly vertically coherent~~ the MTF is vertically coherent in most regions, so here the "local" time series are depth-integrated.

In Figure 12, R_{MTF} is computed such that the local time series is the MTF and the total time series is the total ~~MHT~~

485 meridional HT (sum of all components) at ID timescales with the mean and seasonal cycle removed. These maps show the regions where local MTF has substantial variability that is coherent with total ~~MHT~~ meridional HT variability in a given basin. Overall, three areas emerge where the MTF variability contributes substantially (and positively) to basin-integrated ~~MHT~~ meridional HT variability: the North Atlantic, the tropical Indo-Pacific, and the Southern Ocean between 0°~~-100~~–100°E. In the North Atlantic, the positive contributions peak at $\sim$43°N, where the Grand Banks of Newfoundland protrude into the

490 North Atlantic Current (Figure 12a). In contrast, the "negative" contributions of the Gulf Stream and the Kuroshio south of their separations from the continental shelf imply that MTF variations compensate other components (specifically large-scale temperature fluxes)~~and therefore decrease MHT variability on ID timescales at these latitudes~~. For instance, if the large-scale flow is less efficient than usual at advecting heat poleward (perhaps due to the orientation or intensity of the main current), mesoscale variability may take up more of this flux instead. The tropical Indo-Pacific contributions are highest in the TIW

495 bands (Figure 12b), with a notable asymmetry across the equator: north of the equator the MTF contributes directly to ~~MHT~~ meridional HT variability, while south of the equator the MTF compensates ~~MHT~~ meridional HT variability from other components. In the north equatorial TIW band, the mesoscale contribution to meridional HT contributes to the total meridional
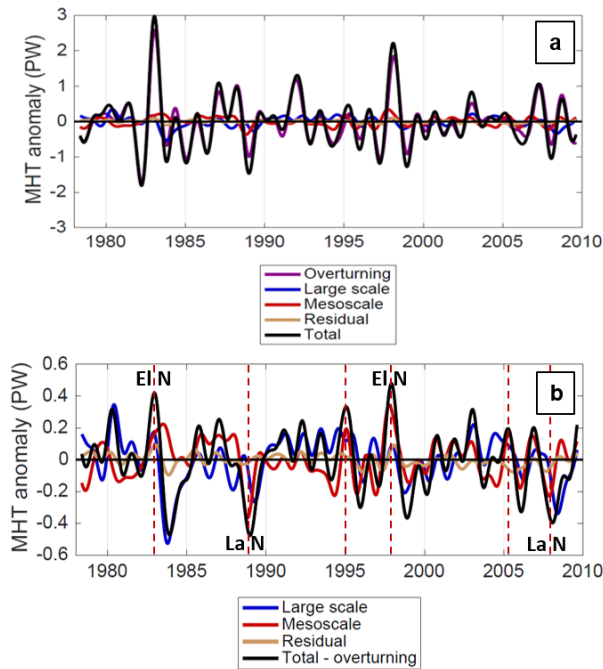
Figure 13. (a) Time series of spatial components of meridional HT variability in the Indo-Pacific basin across 4°N, with time means removed. (b) Same as (a), but with the overturning component of meridional HT variability removed. Vertical red dashed lines indicate episodes where mesoscale MHT drives variations in the total (non-overturning) MHT. Major El Niño (El N) and La Niña (La N) events coincident with mesoscale extrema are also annotated.

HT, often in phase with the much larger overturning contribution (Figure 13); this variability is also closely related to the El Niño-Southern Oscillation. The mesoscale contributions near 13°S (Figure 13a,b) are focused in the Indian Ocean on both the
500 western and eastern sides, though they are weaker than the near-equatorial contributions. In the Southern Ocean, the Agulhas Return Current ~~and lee of the Kerguelen Plateau emerge as hotspots for mesoscale contributions to total MHT (Figure 12c). The largest concentrations of MTF contribution are focused near the Agulhas Retroflection (~~(45°-40°S, 10°-20°E) ~~, and just east of Kerguelen~~ and lee of the Kerguelen Plateau (55°-45°S, 70°-100°E) ~~.~~ emerge as hotspots for mesoscale contributions to total meridional HT (Figure 12c). Among the above areas, there are two regions where the local MTF and basin-integrated
505 total meridional HT are also highly positively correlated with $C(\mathrm{loc}, \mathrm{tot}) > 0.5$: the Pacific TIW region north of the equator, and the lee of the Kerguelen Plateau. The implication is that mesoscale processes in these two regions have a direct impact on the meridional HT at their respective latitudes, without much compensation from the overturning or large-scale contributions.

5.2 Surface EKE as a proxy for ID MTF variability

Local velocity variability and EKE have been considered in previous studies as possible observational proxies for lateral heat fluxes induced by mesoscale eddies (e.g., Stammer, 1998; Bolton et al., 2019; Müller and Melnichenko, 2020). Delman and Lee (2020) explored the degree to which variations in surface EKE can account for MTF variability at ID timescales, along the 40°N transect in the North Atlantic. By applying mixing length theory (e.g., Green, 1970; Holloway, 1986; Stammer, 1998) the relationship can be expressed as

$$\text{MTF} \approx \kappa \frac{\partial T}{\partial y} \tag{12}$$

$$\kappa \propto -\sqrt{v'^2} L_{\text{mix}} \approx -\sqrt{\text{EKE}} L_{\text{mix}} \tag{13}$$

where $\propto$ indicates proportionality (not equality), κ is the diffusivity (which is generally negative or downgradient), and L_{mix} is the mixing length. According to this construct, if the mixing length and meridional temperature gradient do not vary greatly, EKE should be correlated locally with the MTF. In this analysis, the zonal smoothing filter used on MTF in previous figures is applied to both EKE and MTF in order to reduce the impact of shifts in the location of currents and focus on the regional relationship between EKE and MTF.

Figure 14 shows the fraction of MTF variance at ID timescales explained by local variations in the surface EKE; the fraction of variance is equivalent to the squared correlation coefficient of the surface EKE and MTF. Many regions in the ocean have a significant correlation and fraction of variance explained. These areas include the southern excursions of the ACC, the subtropical bands of eddy activity in the Indo-Pacific at $\sim$20°-25° latitude in both hemispheres, and the fringes of energetic western boundary currents. One characteristic shared by these areas is that they tend to have modest levels of time-mean EKE overall (Figure 1); in fact, many of these areas occur near the time-mean contour of 100 cm^2 s^{-2} in the POP model, which often separates energetic and quiescent regions in the ocean.

However, in the core of more energetic regions with high EKE, surface EKE is not a good proxy for the MTF. These energetic regions include the Gulf Stream and Kuroshio extensions as well as the Agulhas Return Current, which are annotated in Figure 14. The lack of significant MTF variance associated with EKE in these high-energy regions may be attributed to several factors. EKE is a convenient and widely-understood metric of mesoscale activity, but it is based on removing a temporal mean from the velocity field and it is not the most precise way to gauge the level of mesoscale energy present. Higher levels of EKE may be associated with an anomalous placement of the current jet and associated front, which does not necessarily change the cross-jet flux. Moreover, strong velocity jets tend to suppress diffusivity across fronts by reducing the mixing length (Ferrari and Nikurashin, 2010); hence variations of the mixing length unrelated to EKE interfere with the relationship between EKE and cross-frontal fluxes. Ultimately the MTF depends not only on the level of mesoscale velocity and temperature variance variation, but on the local correlation between v_M and T_M (Delman and Lee, 2020), and the which in turn is a measure of the efficiency
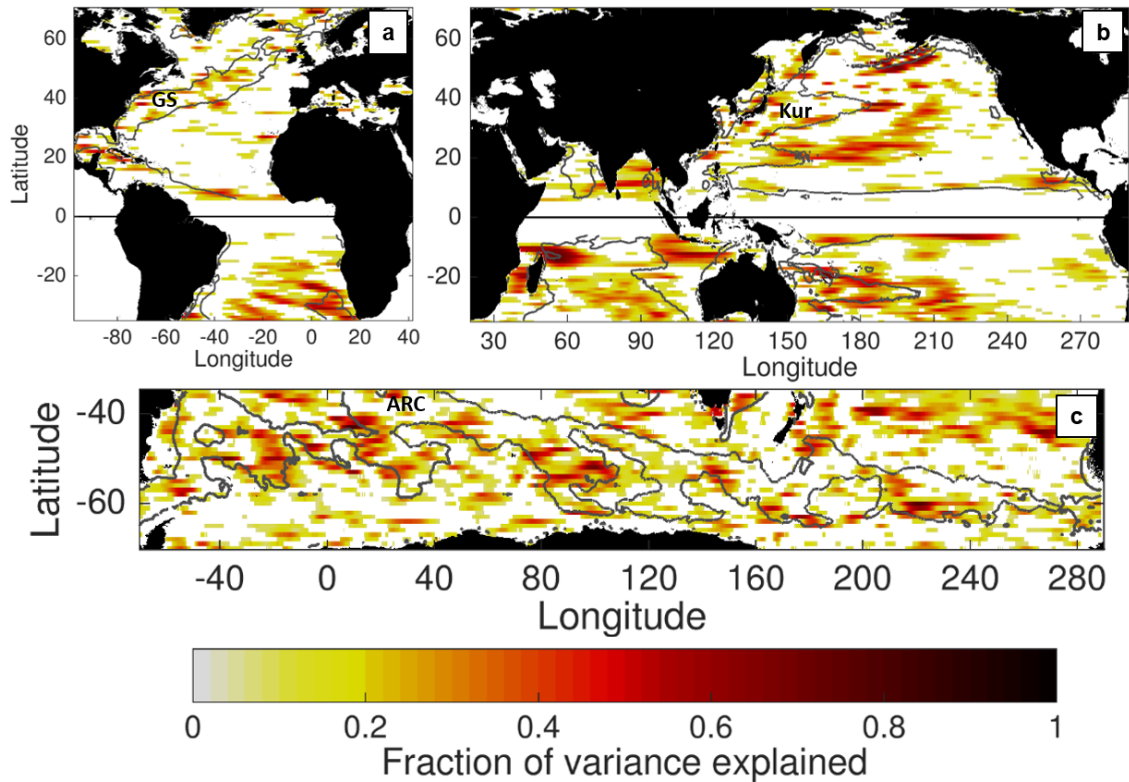
Figure 14. Fraction of zonally-smoothed mesoscale temperature flux variance explained by the regression onto surface EKE, at ID timescales. Only areas with a signal-to-noise ratio > 1 at the 95% confidence level are shaded. The gray contour indicates 100 cm^2 s^{-2} time-mean EKE in the POP model. Several regions (GS, Kur, ARC) with very high time-mean EKE are labeled.

of mesoscale motions in producing a net directional flux. The factors affecting this ~~correlation~~ v_M-T_M correlation locally need

540   to be ~~further explored.~~ investigated more in future work. Figure 14 does however provide an indication of areas of the ocean where surface EKE might be a decent proxy for the MTF, in contrast with the more energetic regions where mixing length and gradient variability can interfere with the EKE-MTF relationship.

6   Conclusions

This analysis uses the method first applied in Delman and Lee (2020) in the North Atlantic to quantify mesoscale temperature

545   fluxes in the global oceans, and their contribution to the time-mean and ID variability of ~~MHT~~meridional HT. The resulting assessment indicates that mesoscale ocean dynamics generally spread heat outward from the subtropics: poleward in mid-latitudes, and equatorward in the tropics. Hence the net effect of the mesoscale ~~MHT~~ meridional HT is to flux heat from where thermocline isotherms are deepest (in subtropical gyres) to where they are shallower, consistent with the "slumping"

associated with typical parameterizations of mesoscale effects in models (e.g., Gent and McWilliams, 1990). Despite this,
mesoscale temperature fluxes do not always act to diminish large-scale horizontal temperature gradients. In the Agulhas and
East Australian Current, mesoscale recirculations act to flux heat equatorward at mid-latitudes (Figure ~~2~~3b), such that the net
mesoscale ~~MHT~~ meridional HT is equatorward at 35°-30°S in the Indo-Pacific (Figure 7c). Moreover, the time variability of
mesoscale temperature fluxes on ID timescales is not well explained by surface EKE variability in the most energetic regions
of the ocean; hence a more nuanced understanding of how mesoscale processes flux heat across strong currents is needed.

It is important to highlight the differences between the definition of the mesoscale flux described here and the "eddy"
fluxes used in other studies, as described in Section 4. While eddy fluxes are typically associated with deviations from
a zonal or temporal mean, neither of these definitions separates the effects of mesoscale phenomena from those of basin
scale gyres or long planetary waves. Moreover, stationary mesoscale recirculations contribute substantially to mesoscale
~~MHT (Figure ??, right column~~meridional HT (Figure 5). The effects of these recirculations are not included in ~~an eddy
flux~~~~based on temporally-varying flow~~a temporally-defined eddy flux, but these recirculations still need to be parameterized
as they will not be accurately simulated in a coarse-resolution (∼1° grid spacing) ocean model. ~~Since spatial rather than
temporal resolution is often the limiting factor in simulating ocean dynamics, flux diagnostics based on spatial scales are
needed to improve model parameterizations~~ By implementing this diagnostic to separate scales in mesoscale-permitting and
mesoscale-resolving simulations, it is possible to better understand how stationary and transient mesoscale phenomena induce
fluxes across large-scale gradients. Future studies can focus on relating large-scale gradients (in one, two, and three dimensions)
to mesoscale diffusivities, and therefore on improving parameterizations of mesoscale impacts from stationary recirculations
as well as ~~to compare mesoscale-permitting model simulations~~propagating eddies.

The scope of this study leaves a number of questions unanswered about the effects of mesoscale dynamics on heat pathways
through the ocean. While POP simulates EKE well in the Southern Ocean and western boundary currents where MTF is
substantial, the model has a low EKE bias in some subtropical and tropical regions (Figure 1). Hence the spatial decomposition
method should be applied in models that simulate mesoscale activity and variability more accurately in these regions. The
large-scale/mesoscale decomposition used in this study is applied only in one dimension (zonally), and therefore does not
separate divergent from rotational fluxes. Only the divergent fluxes contribute to changes in ocean heat content locally, so a
separation of the large-scale and mesoscale in both horizontal dimensions is needed to compute the divergence and assess the
impact of mesoscale dynamics on local heat content. ~~The relationship between MTF variability and other characteristics of the
large-scale and mesoscale state also needs to be investigated more extensively. The~~ Lastly, the disconnect between surface EKE
and MTF variability in the most active mesoscale regions ~~may be the result of~~ also needs further attention, as it may result from
factors such as variability in large-scale temperature gradients, mixing length, and the local geometry of the mesoscale flow
field. Assessing the influence of these factors on MTF variability, perhaps with the aid of more complex statistics and/or deep
learning techniques (George et al., 2019), can be expected to produce improvements in ~~model parameterizations and better
predictive models for tracer fluxes across mesoscale fronts~~predictions of the fluxes associated with mesoscale variability.

Data availability. The POP model output used in this study is stored on NCAR's High Performance Storage System (HPSS); the full model output in 5-day averages is available with a user account (through https://www2.cisl.ucar.edu) by logging into cheyenne.ucar.edu and accessing the following path on HPSS: /home/bryan/johnsonb/g.e01.GIAF.T62_t12.003/ocn/hist/. Source code to run the POP2 model is
585   available at http://www.cesm.ucar.edu/models/cesm1.0/pop2/. The CMEMS surface dynamic topography data used to produce the analysis in Figure 1 are available from http://marine.copernicus.eu/services-portfolio/access-to-products/ by searching for the Product ID SEALEVEL_GLO_PHY_L4_REP_OBSERVATIONS_008_047.

Appendix A: Mesoscale transition scale λ_0

Delman and Lee (2020) used $\lambda_0 = 10°$ longitude as the threshold wavelength in the North Atlantic, based on spectral analyses
590   of meridional velocity and temperature at a range of latitudes. For this study, similar spectral analyses were carried out in the Atlantic, Indo-Pacific, and Southern ocean basins; the meridional velocity spectra are shown at various latitudes in the Indo-Pacific and Southern ocean basins as examples (Figure A1). As in Delman and Lee (2020), the mesoscale/large-scale transition and mesoscale peak wavelengths were estimated from each transect based on the logarithmically-smoothed spectral density profiles. The choice of $\lambda_0 = 10°$ longitude was found to be reasonable at and poleward of 20° latitude. Even where the
595   objectively-identified transition wavelength was very different from 10° (e.g., 20°S in the Indo-Pacific as shown in Fig. A1e), the mesoscale "bump" in the spectra clearly occurs at scales smaller than 10°. The one exception to this pattern is at some tropical latitudes (e.g., 10°S Indo-Pacific, Fig. A1d), where the mesoscale bump extends to scales larger than 10° longitude. Given this, and the abrupt growth of the deformation radius and typical eddy scales equatorward of 20° (Chelton et al., 2011) , the transition wavelength was set to $\lambda_0 = 20°$ longitude within 10° of the equator, $\lambda_0 = 10°$ poleward of 20° latitude in both
600   hemispheres, with a linear transition in λ_0 in the 10°–20° latitude range.

The wavelength (not radius) λ_0 was deliberately chosen to be larger than the size of nearly all eddies, in order to ensure that their signals are retained in the mesoscale. For instance, an eddy radius of 1° longitude and diameter of 2° is typical at mid-latitudes (Chelton et al., 2011), corresponding to a wavelength of 4° longitude. If λ_0 at mid-latitudes is chosen to be 4° or 5° longitude, much of the signal of larger eddies will be included in the large-scale profiles along with basin gyres and long
605   planetary waves. Hence a choice of $\lambda_0 = 10°$ results in a cleaner separation of these phenomena.

Appendix B: Composite adjustment for model EKE bias

The POP model's significant underrepresentation of EKE (Figure 1) in some parts of the ocean is a potential concern for the results of this analysis, in that it may also lead to an incorrect representation of the fluxes and transport associated with oceanic mesoscale activity. This concern is mitigated somewhat by the fact that the low EKE biases tend to occur in calmer interior
610   regions of the ocean where satellite observations agree that EKE is generally lower overall (Figure 1a). Nonetheless, there are areas where observed mesoscale activity is large enough that this bias might impact estimates of meridional HT, especially in the subtropical eddy bands of the Pacific and Indian oceans, and the eddy activity near the Azores Current (∼35°N) in the Atlantic.
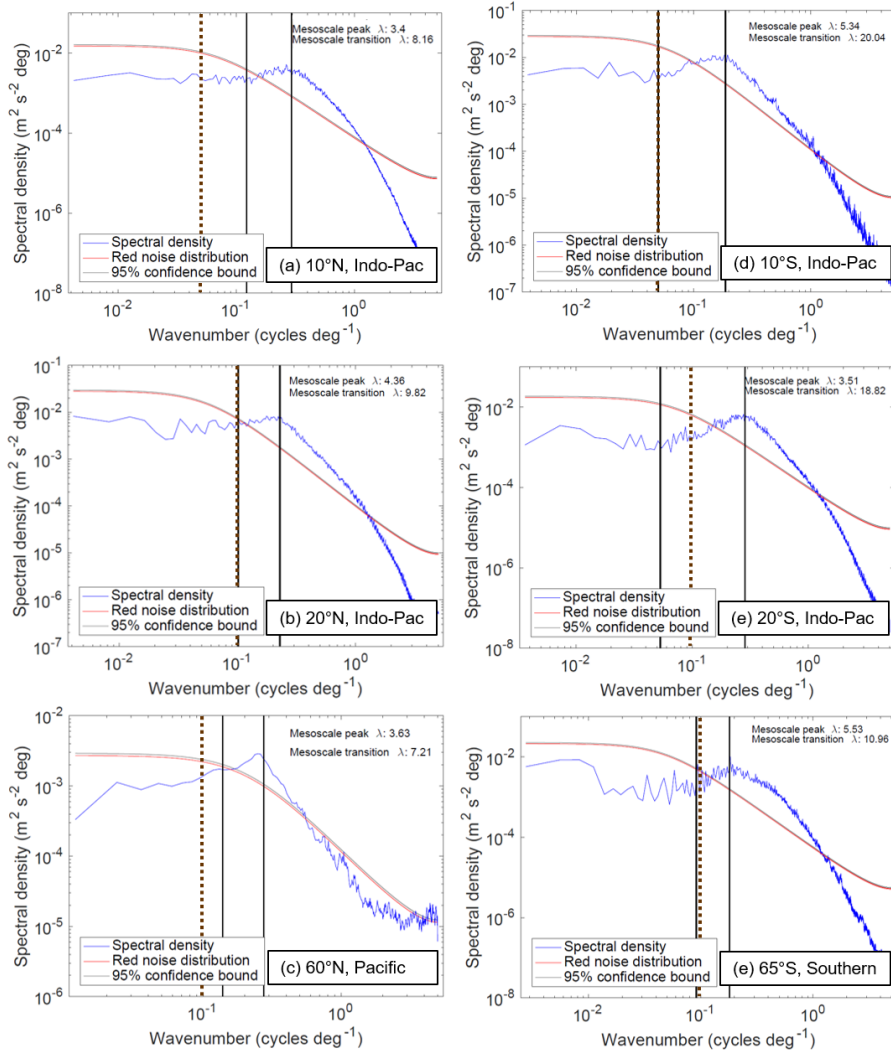
Figure A1. Zonal wavenumber spectral density of meridional velocity in POP, along latitude transects in specified basins. The black vertical lines and small text indicate the wavelength associated with the mesoscale transition and peak, as computed using the logarithmically-smoothed spectral density profile. The vertical dashed brown line indicates the wavelength λ_0 chosen for the mesoscale/large-scale threshold at that latitude. The red and gray curves indicate the red noise distribution expected from lag-1 (model grid-scale) autocorrelation and the corresponding 95% confidence bound.

An imperfect way to get an estimate of the EKE bias's impact on MTF and meridional HT contributions is to construct composite averages of MTF for a given location, in such a way that the model EKE averaged during the composite times is as close as possible to the observed time-mean EKE in that location. In areas where there is a low EKE bias in the model, these
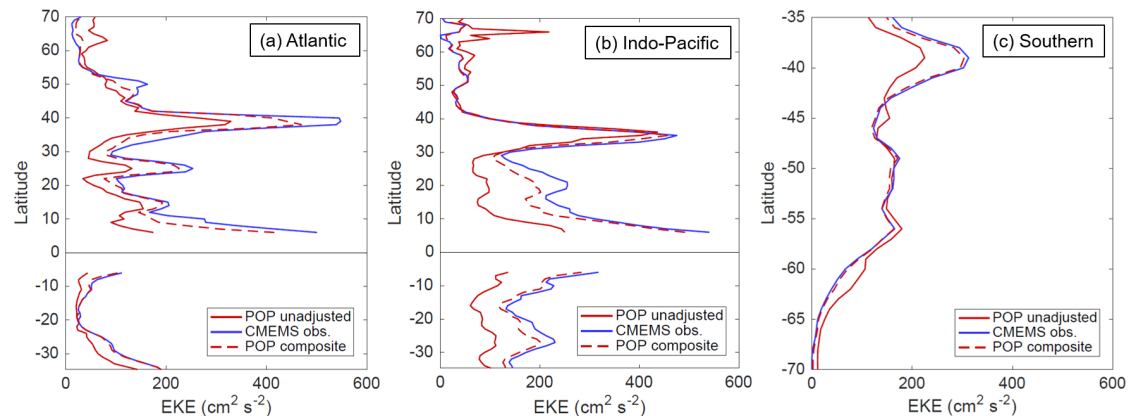
Figure B1. Zonally-averaged surface EKE, in the (a) Atlantic, (b) Indo-Pacific, and (c) Southern ocean basins. The three curves indicate the values from the unadjusted POP simulation, from the CMEMS satellite-based gridded data product, and from the EKE-adjusted composite that is intended to emulate EKE levels in the CMEMS observations.

adjusted composites exclude times when the EKE is lower, in order to average MTF only at times when EKE levels are closer to observations. This is done using values of EKE that are zonally smoothed (in the same way MTF values were smoothed in Figure 2) in order to avoid the method being impacted by minor shifts in current position. One caveat to this approach is that the bias in parts of the subtropics is substantial enough that the observational EKE can not be matched exactly without limiting the composite averages to one or two anomalous events in the model. In this analysis the time range included in each adjusted composite was required to include at least 3 years cumulatively (with any number of gaps), to limit the influence of individual events or eddies. Even with this limitation, the adjusted composite EKE levels are still at least 50% of the observational time-mean in the same location for 92% of the ocean's area studied. Furthermore, the zonally-averaged composite EKE in each basin is closer to observational values than the unadjusted time-mean POP value (Figure B1), everywhere except for a couple of latitudes in the North Atlantic (34°N due to the bias in the Azores Current, 50°N due to the bias in the Northwest Corner of the North Atlantic Current).

Mesoscale temperature fluxes based on these EKE-adjusted composites (Figure B2) imply some enhancements of fluxes relative to the unadjusted values in Figure 2 in the tropical and subtropical Indo-Pacific. These enhancements are evident mostly in the subtropical eddy bands and at the Pacific eastern boundary near Central America. However, the overall patterns of the MTF (and in most areas the MTF magnitudes) are not affected by the adjustment. Furthermore, the MTF was zonally integrated in each basin to determine how the adjusted composites affect meridional HT (Figure B3). At nearly every latitude, the adjustments to meridional HT in the composites are very minor. The most substantive adjustments can be found near the meridional HT transport peaks in the Indo-Pacific tropics (north and south of the equator) and in the Southern Ocean near 40°S; the peaks near Indo-Pacific 13°S and Southern Ocean 40°S are enhanced by 0.1–0.15 PW (Figure B3b,c). Everywhere else, the adjustments are less than 0.1 PW. These results imply that, while the low time-mean EKE bias in the model may have
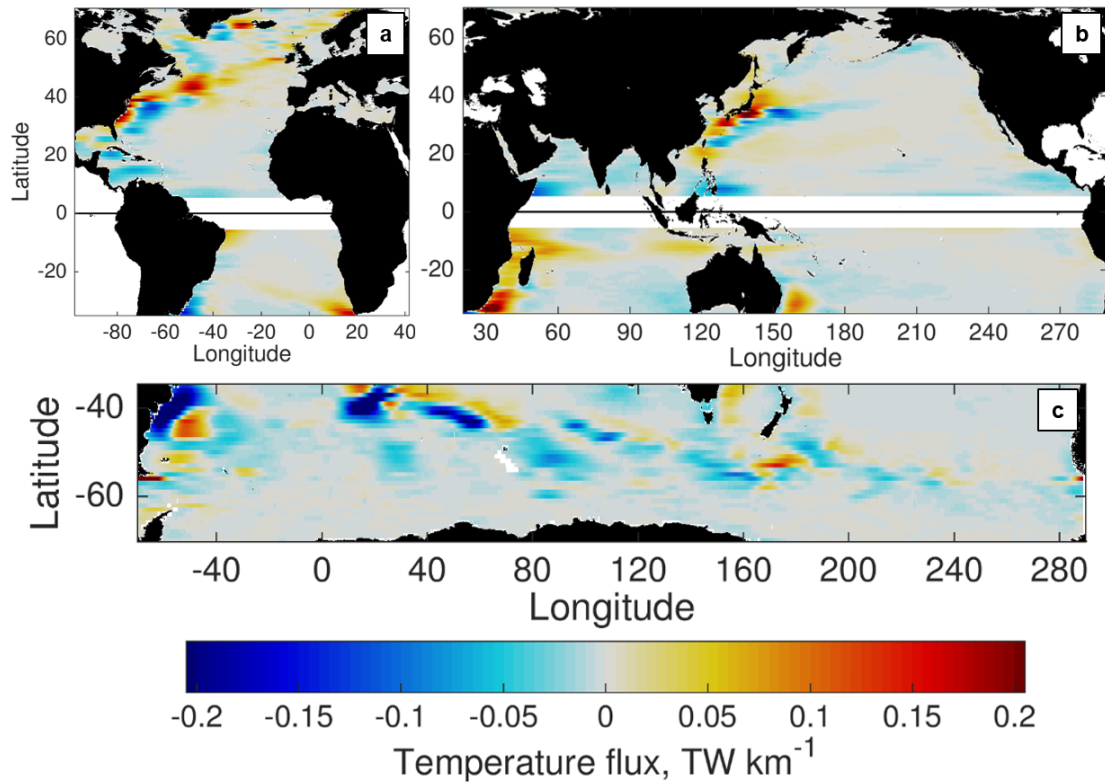
Figure B2. EKE-adjusted composite estimate of time mean zonally-smoothed meridional temperature flux associated with the mesoscale flow. Fluxes shown in the (a) Atlantic, (b) Indo-Pacific, and (c) Southern Ocean basins.

an impact on MTF values in some regions, the overall assessment of mesoscale contributions to meridional HT should not be greatly impacted by these EKE biases that occur mostly in interior ocean regions.

Author contributions. Primary author Andrew Delman wrote the code, carried out the analysis presented, and drafted the manuscript. Tong Lee supervised the project, providing input into the direction of the research and edits to the manuscript.

640

Competing interests. There are no competing interests present in the publication of this paper.
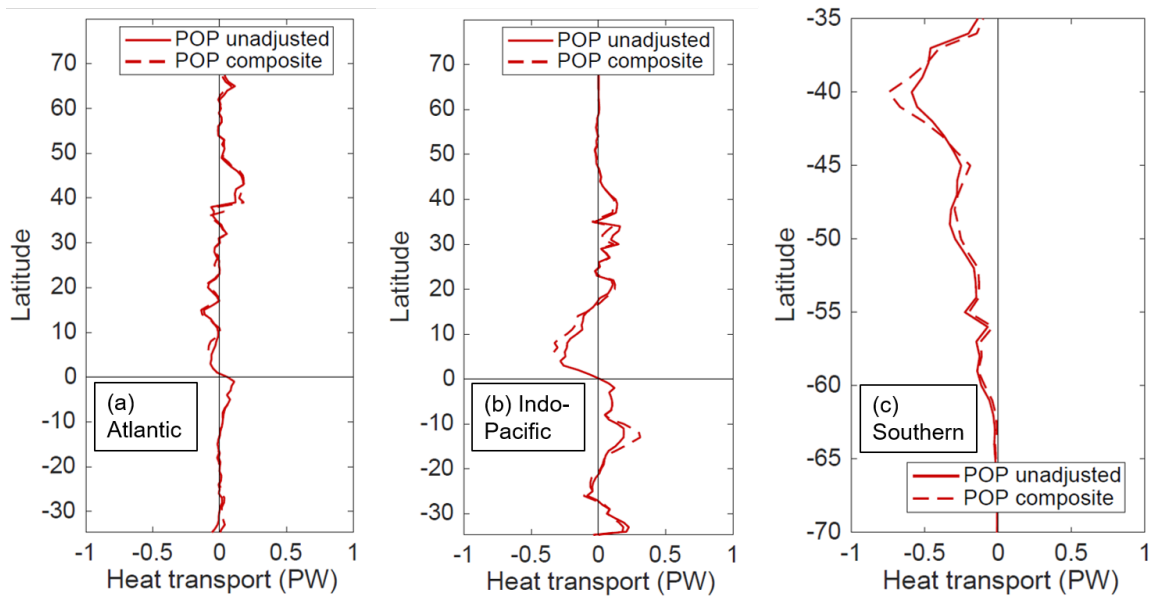
Figure B3. Mesoscale contribution to meridional HT in the (a) Atlantic, (b) Indo-Pacific, and (c) Southern ocean basins. The unadjusted values (corresponding to the red curves in Figure 7) and the values associated with the EKE-adjusted composites are shown at each latitude.

Acknowledgements. The research was carried out at the Jet Propulsion Laboratory, California Institute of Technology, under a contract with the National Aeronautics and Space Administration (80NM0018D004) with the support of NASA Physical Oceanography. The authors would like to acknowledge Benjamin Johnson who ran the POP model configuration and made the output available, as well as Frank Bryan
645   at the National Center for Atmospheric Research who helped us obtain the output. We are also grateful to three anonymous reviewers whose feedback greatly improved this manuscript.

References

Abernathey, R. and Haller, G.: Transport by Lagrangian vortices in the eastern Pacific, Journal of Physical Oceanography, 48, 667–685, 2018.

Aoki, K., Minobe, S., Tanimoto, Y., and Sasai, Y.: Southward eddy heat transport occurring along southern flanks of the Kuroshio Extension and the Gulf Stream in a 1/10° global ocean general circulation model, Journal of Physical Oceanography, 43, 1899–1910, 2013.

Bolton, T., Abernathey, R., and Zanna, L.: Regional and temporal variability of lateral mixing in the North Atlantic, Journal of Physical Oceanography, 49, 2601–2614, 2019.

Boulanger, J.-P. and Menkès, C.: Long equatorial wave reflection in the Pacific Ocean from TOPEX/POSEIDON data during the 1992–1998 period, Climate Dynamics, 15, 205–225, 1999.

Bryan, K.: Poleward heat transport by the ocean: observations and models, Annual Review of Earth and Planetary Sciences, 10, 15–38, 1982.

Chaigneau, A. and Pizarro, O.: Eddy characteristics in the eastern South Pacific, Journal of Geophysical Research: Oceans, 110, 2005.

Charney, J. G. and Stern, M.: On the stability of internal baroclinic jets in a rotating atmosphere, Journal of the Atmospheric Sciences, 19, 159–172, 1962.

Chelton, D. B., Schlax, M. G., and Samelson, R. M.: Global observations of nonlinear mesoscale eddies, Prog. Oceanog., 91, 167–216, 2011.

Computational and Information Systems Laboratory: Yellowstone: IBM iDataPlex System (University Community Computing), Boulder, CO: National Center for Atmospheric Research. http://n2t.net/ark:/85065/d7wd3xhc., 2016.

Cox, M. D.: An eddy resolving numerical model of the ventilated thermocline, Journal of Physical Oceanography, 15, 1312–1324, 1985.

Delman, A. and Lee, T.: A new method to assess mesoscale contributions to meridional heat transport in the North Atlantic Ocean, Ocean Science, 16, 979–995, 2020.

Delman, A. S., McClean, J. L., Sprintall, J., Talley, L. D., and Bryan, F. O.: Process-specific contributions to anomalous Java mixed layer cooling during positive IOD events, Journal of Geophysical Research: Oceans, 123, 4153–4176, 2018.

Dong, C., McWilliams, J. C., Liu, Y., and Chen, D.: Global heat and salt transports by eddy movement, Nature Communications, 5, 1–6, 2014.

Dong, D., Brandt, P., Chang, P., Schütte, F., Yang, X., Yan, J., and Zeng, J.: Mesoscale eddies in the northwestern Pacific Ocean: Three-dimensional eddy structures and heat/salt transports, Journal of Geophysical Research: Oceans, 122, 9795–9813, 2017.

Ducet, N., Traon, P. Y. L., and Reverdin, G.: Global high–resolution mapping of ocean circulation from TOPEX/Poseidon and ERS–1 and –2, J. Geophys. Res., 105, 19,477–19,498, 2000.

Eady, E. T.: Long waves and cyclone waves, Tellus, 1, 33–52, 1949.

Eden, C. and Greatbatch, R. J.: Towards a mesoscale eddy closure, Ocean Modelling, 20, 223–239, 2008.

Ferrari, R. and Nikurashin, M.: Suppression of eddy diffusivity across jets in the Southern Ocean, Journal of Physical Oceanography, 40, 1501–1519, 2010.

Gent, P. R. and McWilliams, J. C.: Isopycnal mixing in ocean circulation models, Journal of Physical Oceanography, 20, 150–155, 1990.

George, T., Manucharyan, G., and Thompson, A.: Deep learning to infer eddy heat fluxes from sea surface height patterns of mesoscale turbulence, 2019.

Greatbatch, R., Zhai, X., Claus, M., Czeschel, L., and Rath, W.: Transport driven by eddy momentum fluxes in the Gulf Stream Extension region, Geophysical Research Letters, 37, 2010.

Green, J.: Transfer properties of the large-scale eddies and the general circulation of the atmosphere, Quarterly Journal of the Royal Meteorological Society, 96, 157–185, 1970.

Griffies, S. M., Winton, M., Anderson, W. G., Benson, R., Delworth, T. L., Dufour, C. O., Dunne, J. P., Goddard, P., Morrison, A. K., Rosati, A., et al.: Impacts on ocean heat from transient mesoscale eddies in a hierarchy of climate models, Journal of Climate, 28, 952–977, 2015.

Hallberg, R.: Using a resolution function to regulate parameterizations of oceanic mesoscale eddy effects, Ocean Modelling, 72, 92–103, 2013.

Hausmann, U. and Czaja, A.: The observed signature of mesoscale eddies in sea surface temperature and the associated heat transport, Deep Sea Research Part I: Oceanographic Research Papers, 70, 60–72, 2012.

Holloway, G.: Estimation of oceanic eddy transports from satellite altimetry, Nature, 323, 243–244, 1986.

Jayne, S. R. and Marotzke, J.: The oceanic eddy heat transport, Journal of Physical Oceanography, 32, 3328–3345, 2002.

Jochum, M. and Murtugudde, R.: Temperature advection by tropical instability waves, Journal of Physical Oceanography, 36, 592–605, 2006.

Johns, W. E., Baringer, M. O., Beal, L., Cunningham, S., Kanzow, T., Bryden, H. L., Hirschi, J., Marotzke, J., Meinen, C., Shaw, B., et al.: Continuous, array-based estimates of Atlantic Ocean heat transport at 26.5 N, Journal of Climate, 24, 2429–2449, 2011.

Johnson, B. K., Bryan, F. O., Grodsky, S. A., and Carton, J. A.: Climatological annual cycle of the salinity budgets of the subtropical maxima, Journal of Physical Oceanography, 46, 2981–2994, 2016.

Large, W. G. and Yeager, S. G.: Diurnal and decadal global forcing for ocean and sea-ice models: the data sets and flux climatologies, NCAR Tech. Note. NCAR/TN-460+STR, 2004.

Large, W. G. and Yeager, S. G.: The climatology of an interannually–varying air sea flux data set, Clim. Dyn., 33, 341–364, 2009.

Laxenaire, R., Speich, S., Blanke, B., Chaigneau, A., Pegliasco, C., and Stegner, A.: Anticyclonic eddies connecting the western boundaries of Indian and Atlantic oceans, Journal of Geophysical Research: Oceans, 123, 7651–7677, 2018.

Laxenaire, R., Speich, S., and Stegner, A.: Agulhas Ring Heat Content and Transport in the South Atlantic Estimated by Combining Satellite Altimetry and Argo Profiling Floats Data, Journal of Geophysical Research: Oceans, 125, e2019JC015 511, 2020.

Marshall, D. P., Maddison, J. R., and Berloff, P. S.: A framework for parameterizing eddy potential vorticity fluxes, Journal of Physical Oceanography, 42, 539–557, 2012.

Marshall, J. and Shutts, G.: A note on rotational and divergent eddy fluxes, Journal of Physical Oceanography, 11, 1677–1680, 1981.

McPhaden, M. J. and Yu, X.: Equatorial waves and the 1997–98 El Niño, Geophysical Research Letters, 26, 2961–2964, 1999.

Müller, V. and Melnichenko, O.: Decadal Changes of Meridional Eddy Heat Transport in the Subpolar North Atlantic Derived From Satellite and In Situ Observations, Journal of Geophysical Research: Oceans, 125, e2020JC016 081, 2020.

Müller, V., Kieke, D., Myers, P. G., Pennelly, C., Steinfeldt, R., and Stendardo, I.: Heat and freshwater transport by mesoscale eddies in the southern subpolar North Atlantic, Journal of Geophysical Research: Oceans, 124, 5565–5585, 2019.

Smith, R., Jones, P., Briegleb, B., Bryan, F., Danabasoglu, G., Dennis, J., Dukowicz, J., Eden, C., Fox-Kemper, B., Gent, P., Hecht, M., Jayne, S., Jochum, M., Large, W., Lindsay, K., Maltrud, M., Norton, N., Peacock, S., Vertenstein, M., and Yeager, S.: The Parallel Ocean Program (POP) reference manual, Tech. Rep. LAUR-10-01853, Los Alamos National Laboratory, and National Center for Atmospheric Research, 2010.

Stammer, D.: On eddy characteristics, eddy transports, and mean flow properties, Journal of Physical Oceanography, 28, 727–739, 1998.

Sun, B., Liu, C., and Wang, F.: Global meridional eddy heat transport inferred from Argo and altimetry observations, Nature Scientific Reports, 9, 1–10, 2019.

Talley, L. D.: Shallow, intermediate, and deep overturning components of the global heat budget, Journal of Physical Oceanography, 33, 530–560, 2003.

Ushakov, K. and Ibrayev, R.: Assessment of mean world ocean meridional heat transport characteristics by a high-resolution model, Russian Journal of Earth Sciences, 18, 2018.

Volkov, D. L., Lee, T., and Fu, L.-L.: Eddy-induced meridional heat transport in the ocean, Geophysical Research Letters, 35, 2008.

Volkov, D. L., Fu, L.-L., and Lee, T.: Mechanisms of the meridional heat transport in the Southern Ocean, Ocean Dynamics, 60, 791–801, 2010.

Wekerle, C., Wang, Q., Danilov, S., Schourup-Kristensen, V., von Appen, W.-J., and Jung, T.: Atlantic Water in the Nordic Seas: Locally eddy-permitting ocean simulation in a global setup, Journal of Geophysical Research: Oceans, 122, 914–940, 2017.

Zhao, J., Bower, A., Yang, J., Lin, X., and Holliday, N. P.: Meridional heat transport variability induced by mesoscale processes in the subpolar North Atlantic, Nature Communications, 9, 1–9, 2018.

725